

1 **Low CCN concentration air masses over the eastern** 2 **North Atlantic: seasonality, meteorology and drivers.**

Robert Wood¹, Jayson D. Stemmler¹, Jasmine Rémillard², Anne Jefferson.³

3 Three key points:

- 4 • A 20 month cloud condensation nuclei (CCN) dataset from the Azores is used to identify
5 air masses with very low concentrations
- 6 • Low CCN air masses tend to occur during winter and spring and are often associated with
7 cold air outbreaks occurring upstream of the Azores
- 8 • Liquid water path enhancement upstream of air mass arrival at the Azores can account for
9 low concentrations via coalescence scavenging

Corresponding author: Robert Wood, Department of Atmospheric Science, University of Wash-
ington, 718 ATG Building Box 351640, Seattle, WA 98195-1640, USA. (robwood2@uw.edu)

¹Department of Atmospheric Science,
University of Washington, Seattle,
Washington, USA.

²Stony Brook University, New York, USA.

³Cooperative Institute for Research in
Environmental Sciences, Boulder, USA.

10 **Abstract.** A 20 month cloud condensation nucleus concentration (N_{CCN})
11 dataset from Graciosa Island (39°N, 28°W) in the remote North Atlantic is
12 used to characterize air masses with low CCN concentrations. Low CCN events
13 are defined as 6 hour periods with mean $N_{\text{CCN}} < 20 \text{ cm}^{-3}$ (0.1% supersat-
14 uration). A total of 47 low CCN events are identified. Surface, satellite and
15 reanalysis data are used to explore the meteorological and cloud context for
16 low CCN air masses. Low CCN events occur in all seasons, but their frequency
17 was three times higher in Dec-May than during Jun-Nov. Composites show
18 that many of the low CCN events had a common meteorological basis that
19 involves southerly low level flow and rather low wind speeds at Graciosa. Anoma-
20 lously low pressure is situated to the west of Graciosa during these events,
21 but back-trajectories and lagged SLP composites indicate that low CCN air
22 masses often originate as cold air outbreaks to the north and west of Gra-
23 ciosa. Low CCN events were associated with low cloud droplet concentra-
24 tions (N_d) at Graciosa, but liquid water path (LWP) during low CCN events
25 was not systematically different from that at other times. Satellite N_d and
26 LWP estimates from MODIS collocated with Lagrangian back-trajectories
27 show systematically lower N_d and higher LWP several days prior to arrival
28 at Graciosa, consistent with the hypothesis that observed low CCN air masses
29 are often formed by coalescence scavenging in thick warm clouds, often in
30 cold air outbreaks.

1. Introduction

31 Cloud condensation nuclei (CCN) influence the radiative budget of the earth through
32 their activation to cloud droplets, the concentration of which (N_d) is a key determinant of
33 cloud effective radius and therefore cloud optical thickness and albedo [*Boers and Mitchell,*
34 1994]. In many regions, the CCN concentration (N_{CCN}) has increased considerably over
35 the industrial period [*Isaksen et al., 2009*], and is thought to have led to an increase in cloud
36 albedo, but the magnitude of the radiative forcing (RF_{aci}) from aerosols via these aerosol-
37 cloud interactions is highly uncertain [*IPCC, 2013*]. Theoretical and modeling results
38 show that the change in albedo associated with an increase in CCN is dependent not only
39 upon the CCN perturbation, but also upon N_{CCN} in the unperturbed state [*Carshaw et al.,*
40 2013]. This is both because the albedo of a cloud with a very low N_d is more susceptible
41 to N_d increases than is the albedo of a cloud with a higher unperturbed N_d [*Platnick*
42 *and Twomey, 1994*], and also because the relationship between N_{CCN} and N_d is concave
43 [*Martin et al., 1994; Ramanathan, 2001; Hudson et al., 2010*]. These arguments support
44 the notion that albedo responses are strongly sublinear to emissions [*Carshaw et al., 2013*],
45 although there are conflicting results regarding this degree of sublinearity [*Ghan et al.,*
46 2013]. Nevertheless, both *Carshaw et al.* [2013] and *Ghan et al.* [2013] demonstrate that a
47 large fraction of the uncertainty in RF_{aci} can be attributed to uncertainty in the aerosol
48 state of the preindustrial environment.

49 Recent studies have questioned the extent to which the present day aerosol environment
50 is pristine, i.e., unperturbed by anthropogenic impacts and therefore representative of
51 preindustrial conditions. *Andreae* [2007] argues that unperturbed regions may be difficult

52 to find in the Northern Hemisphere (NH), even over the oceans, and observational evidence
53 at remote marine locations provides some support for this *Hudson and Noble* [2009];
54 *Clarke et al.* [2013]. *Hamilton et al.* [2014] quantified the degree of pristineness by using
55 preindustrial and present day emissions in two simulations of a global model, forced with
56 identical meteorology, to identify the fraction of days on which low-altitude N_{CCN} in the
57 preindustrial and present day differ by more than 20%. Over the NH oceans, their results
58 indicate very few days that are pristine by this metric. Curiously, the few pristine days
59 that do occur over the NH oceans in their model occur in summertime, when observations
60 suggest higher N_{CCN} than during winter [*Wood et al.*, 2015]. There is not necessarily
61 a conflict here, however, because low concentrations are not, by themselves, necessarily
62 indicative of pristineness. That said, it is reasonable to imagine that in many instances
63 low N_{CCN} is likely to be indicative of a lack of pollution aerosol. Further, as it is not
64 possible to observe the preindustrial aerosol environment directly, it seems important to
65 devote attention to low CCN environments and the processes controlling them.

66 Observations from many marine boundary layers (MBLs) show that there is a large de-
67 gree of spatiotemporal variability in N_{CCN} and N_{d} in the MBL [e.g., *Martin et al.*, 1994;
68 *Heintzenberg et al.*, 2000; *Miles et al.*, 2000; *Allen et al.*, 2011]. The causes of this variabil-
69 ity remain poorly understood, particularly the extent to which sources or sinks control the
70 variability. During certain meteorological conditions it is clear that precipitation-driven
71 removal of cloud droplets (and hence CCN) can dramatically reduce CCN concentrations
72 over mesoscale regions [*Wang et al.*, 2010; *Terai et al.*, 2014; *Berner et al.*, 2013; *Goren*
73 *and Rosenfeld*, 2015], which can introduce considerable temporal and spatial variability.
74 Theoretical and modeling studies [e.g., *Feingold et al.*, 1996; *Mechem et al.*, 2006; *Wood*,

2006] demonstrate that coalescence scavenging, i.e., the removal of cloud droplets by collision-coalescence, is a key mechanism for CCN removal from the MBL. Observational evidence also supports this [Hudson et al., 2015]. Some studies argue that this mechanism may be important for explaining land-ocean CCN contrasts [Baker and Charlson, 1990] and geographical variability of time-mean N_{CCN} over oceans [Wood et al., 2012]. Further, it is clear that the rate of loss of N_{CCN} by coalescence scavenging increases strongly with the availability of liquid water [Feingold et al., 1996; Wood, 2006]. Coupling these findings with the observed dependence of precipitation rate on cloud liquid water path (LWP) and cloud thickness [e.g., Comstock et al., 2004; VanZanten et al., 2005] it has been shown that MBL-averaged loss rates from coalescence scavenging are approximately proportional to the square of the LWP (or the fourth power of cloud thickness), such that CCN rates are negligible for $\text{LWP} < 50 \text{ g m}^{-3}$, but become comparable to surface and entrainment CCN sources for $\text{LWP} \sim 100 \text{ g m}^{-3}$, and are dominant CCN sinks ($\sim 100 \text{ cm}^{-3} \text{ day}^{-1}$) for $\text{LWP} > 200 \text{ g m}^{-3}$ [Wood, 2006].

There has been little systematic study of low N_{CCN} conditions to explore the factors controlling CCN variability in the clean MBL. We know that catastrophic reductions in CCN can occur and that these can help drive cloudiness transitions in the Tropical and subtropical MBL, e.g. closed to open mesoscale cells [Berner et al., 2013]. There is evidence of similar behaviors in midlatitudes [Wood et al., 2015], and very low N_{d} concentrations ($< 20 \text{ cm}^{-3}$) have been observed in subtropical and midlatitude stratocumulus [Hindman et al., 1994; Boers et al., 1998], in cold air outbreaks [Field et al., 2014] and in the high Arctic [Mauritsen et al., 2011]. Twomey and Wojciechowski [1969] examined a large amount of aircraft-derived CCN data over the remote oceans and found a typical

98 timescale of three days for the relaxation of the CCN population to the low values typical
99 of remote marine air, and *Goren and Rosenfeld* [2015] provide a recent detailed satellite
100 case study of the transition from a continental to a marine air mass over the eastern At-
101 lantic showing how the cloud droplet concentration N_d decreases in low clouds advecting
102 from the continent due to coalescence scavenging.

103 In this study, we take advantage of a long, continuous record (20 months) of CCN and
104 other aerosol and cloud datasets at a remote North Atlantic island site that straddles the
105 boundary between the subtropics and the midlatitudes. We focus on exploration of the
106 meteorological and cloud conditions associated with low N_{CCN} events at the site. Section
107 2 describes the datasets to be used and the methodology for case selection. Section 3
108 presents a composite analysis of meteorological conditions for the low N_{CCN} cases, and
109 section 4 provides an analysis of the multi-day Lagrangian history of low N_{CCN} air masses
110 reaching the site. Section 5 discusses potential mechanisms for low CCN events, section 6
111 introduces a conceptual model, and section 7 provides conclusions and suggestions for
112 further study.

2. Data and Methodology

113 At the core of this analysis are data from the 20-month Clouds, Aerosol, and Precipi-
114 tation in the Marine Boundary Layer (CAP-MBL) field deployment of the ARM Mobile
115 Facility (AMF) on Graciosa Island in the Azores [*Wood et al.*, 2015]. The facility operated
116 from April 2009 until December 2010 and provided a number of important *in situ* and
117 surface-based remote sensing observations. Details of the specific datasets used can be
118 found in section 2.1. In addition to the AMF site products, we use meteorological reanal-
119 yses from the ERA-interim product (described in section 2.2), 8-day back trajectories to

120 provide information on air mass histories (section 2.3), and satellite data from the MODIS
121 instrument aboard the NASA Aqua and Terra satellites to provide larger spatial context
122 of the cloud properties (section 2.4).

2.1. AMF Data

123 The CAP-MBL field deployment of the AMF provided a wealth of data from Graciosa
124 island (39.1°N, 28.0°W), a small island in the Azores archipelago situated in the remote
125 eastern North Atlantic approximately 1600 km west of Lisbon, Portugal and roughly
126 4200 km east of Washington, DC. Table 1 details the measurements and instruments used
127 in this analysis.

2.1.1. CCN, CN and aerosol scattering

129 Several *in situ* aerosol measurements from the AMF Aerosol Observing System (AOS)
130 are used in this study. The key variable used to define events in this study is the CCN
131 concentration. CCN measurements are made using a commercially-available Droplet Mea-
132 surement Technologies (DMT) Model 1 CCN counter [Roberts and Nenes, 2005], which
133 measures the N_d at seven supersaturations S (nominally 0.1, 0.2, 0.4, 0.6, 0.9, 1.1 and
134 1.2%). The counter is programmed to step through the different S and varies them by
135 varying the temperature of the chamber walls, with a complete cycle of all seven S made
136 every 30 minutes. S is calculated using a heat transfer and fluid dynamics flow model
137 [Lance *et al.*, 2006]. To ensure the highest quality CCN measurements, we only include
138 data for those times when the instrument temperature, and hence S , is stable. Stable
139 measurements in each S step are averaged together to generate one CCN “measurement”
140 at each S approximately every 30 minutes. The CCN instrument was serviced and cal-
141 ibrated at the beginning the AMF deployment. During the early part of the CAP-MBL

142 campaign the CCN counter appeared to function correctly, but during late 2009 and early
143 2010 it was clear that the CCN counts were decreasing at a rate that seemed suspiciously
144 large. A time series of monthly mean N_{CCN} (Fig. 1) indicates that N_{CCN} began to
145 decrease after September 2009 and continued to decrease until the problem was noticed
146 in June 2010, after which the CCN instrument was thoroughly serviced and calibrated
147 and the concentrations returned to values typical of the same time during the previous
148 year. Because the decline was gradual, the problem was not identified for several months.
149 Despite this, an approach was developed to correct the CCN data using the CN counter
150 as a reference. This correction is described in the Appendix, and only corrected CCN
151 data are used in this study.

152 In addition to N_{CCN} , we use CN concentration N_{CN} measurements from a TSI 3010
153 model collocated with the CCN counter that provides the concentration of all particles
154 greater than approximately 10 nm in diameter. We also use *in situ* aerosol scattering
155 measurements from the AOS nephelometer system, which is collocated with the CCN
156 counter and measures total dry aerosol scattering at three wavelengths. In this study, we
157 use the submicron and sub-10 μm (total) aerosol scattering coefficient at 450, 550 and
158 700 nm wavelength.

159 **2.1.2. Surface wind and cloud measurements**

160 Surface wind direction and speed measurements are made at a altitude of 10 m above
161 ground at the Graciosa site using an RM Young propeller and vane anemometer system
162 (Table 1). We use these data to contrast the wind speed and direction for low N_{CCN}
163 events with those for non-low N_{CCN} conditions.

164 In this study, we use surface remotely-sensed LWP retrievals based on the algorithm
165 developed by *Turner et al.* [2007] that uses the 23.8 and 31.4 GHz channels from the
166 passive microwave radiometer (MWR) situated at the Graciosa site. The LWP retrievals
167 used are from the entire deployment, and have a time interval that is typically 20-30
168 seconds. In this study, we use the LWP retrievals to produce a comparison of the PDFs
169 for low N_{CCN} events with those at other times.

170 Cloud boundaries and types are taken from the hour cloud product described in
171 *Rémillard et al.* [2012]. Cloud types are based on data from the zenith-pointing ARM
172 W-band (95 GHz) cloud radar and a Vaisala lidar ceilometer (model CT25K prior to
173 mid-July 2010, and a model CL31 after that). In this study we use the occurrence of four
174 basic cloud types: high clouds with bases above 7 km; mid-level cloud layers with bases
175 at altitudes of 3-7 km; low-level clouds with bases and tops below 3 km; deep boundary
176 layer clouds, with bases below 3 km but cloud tops above 3 km [see Table 2 in *Rémillard*
177 *et al.*, 2012].

2.2. Meteorological analyses

178 Horizontal wind, pressure and temperature fields from the ERA-interim reanalysis [*Dee*
179 *et al.*, 2011] are used to assess aspects of the large scale meteorological fields associated
180 with low CCN events. In this study we use reanalysis fields every 6 hours (at 00, 06, 12
181 and 18 UTC). Note that at the Azores, local and UTC time are within an hour of each
182 other (local time = UTC -1 hr). These are used to illustrate individual events and to
183 create composite fields for all low CCN events, allowing us to contrast the composite me-
184 teorology with the seasonally-varying mean meteorology. Anomalies for an instantaneous
185 meteorological field are determined by subtracting a 30-day centered running mean field.

186 These allow us to better isolate the synoptic meteorological differences associated with
 187 low CCN events; without taking anomalies, because low CCN events tend to occur during
 188 certain seasons, composite absolute rather than anomalous field may reflect the seasonal
 189 cycle rather than the key synoptic meteorology.

190 Using the ERA-interim reanalyses, we also calculate the marine cold air outbreak
 191 (MCAO) index μ defined in *Kolstad and Bracegirdle* [2007] and *Kolstad et al.* [2009]
 192 as

$$\mu = \frac{\theta_{SST} - \theta_{700}}{p_0 - p_{700}} \quad (1)$$

193 where θ_{SST} is the potential temperature derived from the sea-surface temperature (SST),
 194 θ_{700} is the potential temperature at 700 hPa altitude, p_0 is the sea level pressure, and
 195 $p_{700} = 700$ hPa. The MCAO index defined in (1) is calculated every 6 hours at the times
 196 that ERA-interim data are available. Larger values of μ indicate weaker lower tropospheric
 197 stability, consistent with cold lower tropospheric air overlying a warmer surface. Positive
 198 values of μ are often taken as being indicative of cold air outbreak conditions [*Kolstad*
 199 *et al.*, 2009].

2.3. Trajectories

200 Three dimensional 8-day back trajectories were computed four times daily for the
 201 entire AMF deployment using the full 3D NOAA HYSPLIT trajectory model [*Drax-*
 202 *ier and Hess*, 1998]. Back trajectories end at 500 meters above sea level at Graciosa
 203 at 03, 09, 15, 21 UTC, i.e., at the midpoint of each 6-hour period used to aggregate the
 204 CCN data (see section 3 below) and are constructed for every 6 hour period during the

205 deployment. The trajectories are driven by the NCEP Global Data Assimilation reanal-
206 ysis product at $1\times 1^\circ$ resolution [Kalnay *et al.*, 1996]. Back trajectories provide a more
207 comprehensive understanding of the air masses along their path to the Azores. Meteorolo-
208 gical analysis data, especially the MCAO index (section 2.2), are also interpolated onto
209 the trajectories as a function of time to provide a time history of the Lagrangian evolution
210 of meteorology along trajectories.

2.4. Satellite Datasets

211 Satellite data are taken from the Moderate Resolution Imaging Spectroradiometer
212 (MODIS) on both the NASA Aqua and Terra satellites, which pass over Graciosa at
213 approximately 10:30am and 1:30pm local time. Only daytime data are used. We use
214 daily level 3 products [Oreopoulos, 2005] for each satellite, which aggregate MODIS col-
215 lection 5 retrievals of LWP and effective radius for liquid-topped cloud [King *et al.*, 1997]
216 to a $1\times 1^\circ$ spatial grid. These products are then used to compute droplet number concen-
217 tration N_d at $1\times 1^\circ$ applying the method of Boers *et al.* [2006] and Bennartz [2007], with
218 assumptions detailed in appendix A of Grosvenor and Wood [2014]. To mitigate known
219 problems with retrievals in broken or ice cloud conditions, N_d data are accepted only for
220 those $1\times 1^\circ$ boxes where the total cloud fraction is equal to the single layer liquid cloud
221 fraction and exceeds 60%.

222 We then spatiotemporally collocate the MODIS level 3 data with the back-trajectory
223 locations (section 2.3) to produce a sparse time series of MODIS retrieved properties along
224 the path of each trajectory. To constitute a match in time and space between the satellite
225 data and trajectories, we search for available MODIS data within a $3\times 3^\circ$ box around
226 the trajectory location at the times of the MODIS overpasses. Any level 3 box within

227 this range is considered to be associated with the trajectory. The resulting MODIS time
 228 series are composited as a function of time prior to the air mass arrival at Graciosa, and
 229 this compositing is carried out separately for trajectories that end at Graciosa during low
 230 N_{CCN} and non-low N_{CCN} events, which allows us to contrast the liquid cloud property
 231 histories for these subsets.

3. Composite Analysis of Low CCN Events

232 In this section we define the low CCN events and then composite these events to identify
 233 meteorological properties associated with the events. We compare the composite meteo-
 234 rology with all the data to understand differences between low CCN events and non-low
 235 CCN cases. To define low CCN events, we first average N_{CCN} for S s from 0.0-0.15%
 236 over six hour periods (0-6, 6-12, 12-18, 18-24 UTC). Most of the measurements in this
 237 0.0-0.15% S range are made at a S close to 0.1% (95% of the individual S values range
 238 from 0.11 to 0.125%). This 6-hour mean time series we term $\overline{N_{\text{CCN},0.1\%}}$. Any given 6-hour
 239 period is defined to be a low CCN event if $\overline{N_{\text{CCN},0.1\%}} < 20 \text{ cm}^{-3}$. We use 6-hour periods
 240 as this is sufficiently long to provide a characterization of N_{CCN} in an air mass, while
 241 being short enough to capture variations in air mass properties. Using this definition,
 242 we identify a total of 47 low CCN events. These events constitute approximately 2% of
 243 the total number of 6-hour periods (of which there are 2262 with CCN data, and 223
 244 periods with missing data). Of the 47 low CCN periods identified, 22 are isolated 6-hour
 245 periods, 8 consist of two consecutive 6-hour periods, and 3 consist of three consecutive
 246 6-hour periods. The distribution of N_{CCN} measurements (taken approximately every 30
 247 mins as described in section 2.1.1) at 0.1% S during low CCN events is contrasted with
 248 the distributions for non-low events (Fig. 2). The median $\overline{N_{\text{CCN},0.1\%}}$ is approximately a

249 factor of four higher during non-low CCN events than during low CCN events. We choose
250 to focus on a relatively small set of 33 extreme events here to provide a manageable set
251 of cases that can be explored both individually and statistically.

252 Low CCN events were much more common during winter (DJF) and spring (MAM) than
253 during summer (JJA) and autumn (SON) as shown in Fig. 3. Almost three-quarters of
254 the low CCN events during the deployment occurred during winter and spring, despite
255 the lower availability of data from these seasons due to the deployment not sampling a
256 complete two year period. Factoring out the greater data availability in some seasons, it
257 is three to four times more likely for a low CCN event to occur during winter and spring
258 than it is during summer and autumn (Fig. 3). This preference for winter and spring did
259 not simply track the seasonal mean (or median) N_{CCN} , which did not vary particularly
260 strongly across seasons. Median CCN concentrations $N_{\text{CCN},0.1\%}$ for all data are 60, 78, 80,
261 and 79 cm^{-3} for DJF, MAM, JJA and SON respectively. So although median wintertime
262 $N_{\text{CCN},0.1\%}$ was lower than it was during other seasons, springtime median $N_{\text{CCN},0.1\%}$ was
263 as high as the medians for summer and autumn. This finding is reconciled because the
264 spread of N_{CCN} during spring is larger than that during summer and fall, allowing there
265 to be more low CCN events without a major change in the median concentration.

266 After dividing the 6-hour periods into two categories (low CCN events and non-low
267 CCN periods) we examine a variety of *in situ* and large scale meteorological variables and
268 examine any clear differences that exist between the subsets.

3.1. Aerosol Scattering

269 As with the CCN data, mean submicron dry scattering coefficient at 550 nm is deter-
270 mined for the same 6-hour periods, and these are composited for low CCN and non-low

271 CCN events. Figure 4 shows monthly mean aerosol scattering coefficients for the low
272 and non-low CCN cases, clearly demonstrating a major and systematic reduction in both
273 fine and coarse mode aerosol scattering during low CCN events in all months. The rela-
274 tive reduction of aerosol scattering during low CCN events (compared with non-low CCN
275 events) appears to be roughly proportional to the reduction in N_{CCN} itself, and is not
276 strongly wavelength dependent (Fig. 5). Median scattering is approximately a factor of
277 3 to 4 lower during low CCN events than for non-low events, which is close to the factor
278 of four difference in $N_{\text{CCN},0.1\%}$ (Fig. 2). The similar relative suppressions of scattering
279 and $N_{\text{CCN},0.1\%}$ during low CCN events is consistent with the general relationship between
280 dry scattering and N_{CCN} observed at a number of different continental and marine sites
281 [Jefferson, 2010; Shinozuka et al., 2015].

282 Aerosol scattering is often used as a proxy for N_{CCN} [e.g., Shinozuka et al., 2015]. We
283 conducted tests to explore the use of the submicron dry scattering coefficient at 450 nm
284 wavelength ($\sigma_{450,\text{sub}}$) as an alternative approach to define “low scattering” events in place
285 of the CCN observations. Scattering and N_{CCN} are well correlated. The correlation co-
286 efficient r between 6 hour mean $\sigma_{450,\text{sub}}$ and N_{CCN} is $r = 0.76$ (0.1% S) and $r = 0.71$
287 ($S=0.4\%$). Defining low scattering events as those with 6 hr mean $\sigma_{450,\text{sub}} < 1.5$ (Mm)⁻¹,
288 we identify a similar number of events (53 total). Of these events, 20 of them are identical
289 periods to those identified as low CCN events, and a further 13 are periods that adjoin
290 low CCN periods. As with low CCN events, low scattering events occur most frequently
291 in winter. The largest difference in the seasonality occurred in spring, during which time
292 there were few low scattering events but a considerable number of low CCN events (not
293 shown). We note that spring 2010 is when the correction made to CCN concentrations

294 was the largest (see Appendix), and so differences may reflect lingering issues with the
295 CCN data or may reflect physical differences between scattering and N_{CCN} . Comparisons
296 of meteorological data show that low scattering events had similar wind roses and me-
297 teorological composite fields to those derived from low CCN events (not shown). The
298 findings are also not strongly sensitive to the choice of S used for the CCN measurement.
299 Thus, the key conclusions of this study are largely robust to the specific choice of aerosol
300 data used to define events.

3.2. Meteorology

301 In this section we examine two meteorological components; surface winds and sea-
302 level pressure. These provide some preliminary insight into the history and path of the
303 air masses prior to reaching the Azores. Surface winds and mean sea-level pressure are
304 analyzed using both *in situ* observations as well as model reanalysis data to provide a
305 large-scale picture of these variables.

306 One of the clearest examples of meteorological differences between low CCN events
307 and non-low CCN cases at Graciosa is in the surface (10 m) winds (Fig. 6). Surface
308 winds during low CCN events are considerably weaker and more southerly than at most
309 other times. The median wind speed during low CCN events was 3 m s^{-1} compared with
310 almost 5 m s^{-1} for non-low events. The low wind speeds during low CCN events would
311 be associated with weaker sea-spray particle fluxes [Lewis and Schwartz, 2004], and this
312 may help explain why the total aerosol scattering, with a significant contribution from the
313 coarse mode, was also lower during these periods. However, the clear distinction in wind
314 *direction* suggests that air mass history may also be relevant. We return to the possible
315 mechanisms causing low CCN events in section 5.

316 To further assess the large-scale meteorological conditions associated with low CCN
317 events, we composite ERA-Interim reanalysis surface winds and mean sea-level pressure
318 (MSLP) fields for low CCN events (Fig. 7). At the start of low CCN events (Fig. 7d),
319 Graciosa was typically situated under conditions of large scale southerly flow, a picture
320 consistent with the wind roses (Fig. 6). However, the SLP anomalies at the times of the
321 events alone present a misleading idea of the air mass origins. For several days prior to
322 the low CCN events, the average flow tends to be quite zonal (Fig. 7a,b,c), with a broad
323 area of low pressure from 40-55°N and 30-70°W. During the winter months, air flowing
324 off the North American continent will be cold and will therefore likely experience strong
325 surface temperature increases as it flows over the relatively warmer water of the North
326 Atlantic.

327 However, because low CCN events tend to occur more frequently during certain sea-
328 sons (Fig. 3), the absolute MSLP composite maps potentially alias in the large scale
329 seasonal variability and may not reflect synoptic events. Thus, we also examine compos-
330 ite differences (low CCN events - non-low CCN cases) with the seasonal cycle removed
331 (see section 2.2). Figure 8 shows that at the start of the low CCN events, on average
332 there was an anomalous surface low center to the northwest of Graciosa and a high pres-
333 sure center to the east and north. The anomalously low surface pressure also extended
334 down the entire North American eastern seaboard. The SLP anomalies prior to the low
335 CCN events (Fig. ??a-c) were generally smaller in magnitude and spatial scale, and did
336 not persist from day to day, other than anomalously low pressure consistently along the
337 Eastern seaboard of North America. This indicates that the absolute MSLP composite

338 maps (Fig. 7) provide a reasonable assessment of the mean synoptic flow during low CCN
339 events.

3.3. Cloud properties

340 We examine some of the major cloud properties associated with low CCN events at the
341 Graciosa site. There is little to distinguish distributions of LWP during low CCN events
342 from distributions at other times (Fig. 9), suggesting that cloud differences local to the
343 island and during the events themselves may not play a significant role in driving low CCN
344 events. Distributions of LWP for different seasons show some differences between low and
345 non-low CCN events, but there is no systematic difference across seasons, indicating no
346 clear association between local LWP at Graciosa and the occurrence of low CCN events
347 (Fig. 9).

348 Cloud fraction histograms observed from the ground at Graciosa for low CCN events are
349 contrasted with those for non-low CCN cases in Fig. 10. Hourly cloud fraction histograms
350 are shown for the four cloud types (see section 2.1.2) and for the overall cloud cover (right
351 panels). Statistically, both low and non-low CCN events show similar distributions of
352 cloud cover for various cloud types, but there are some differences. There is a somewhat
353 lower fraction of exclusively boundary layer clouds at Graciosa during low CCN events,
354 but there is a higher fraction of deep boundary layer clouds, mid-level clouds and cirrus,
355 all of which are associated with frontal systems in this region. This seems consistent with
356 there generally being a low pressure situated to the north and west of Graciosa during
357 low CCN events.

358 Although the contrasts between cloud macrophysical variables at Graciosa during low
359 CCN events and other times is muted, N_d from the NDROP data product [*Riihimaki*

360 *et al.*, 2014; *McComiskey et al.*, 2009] measured from surface remote sensing over Graciosa
361 (Fig. 11) are markedly lower during low CCN events than at other times. During low
362 CCN events, there is only a 5% chance that the 6-hour median N_d will exceed 100 cm^{-3} ,
363 whereas a high N_d tail extends to almost 400 cm^{-3} at other times. The median N_d during
364 low CCN events is approximately three times lower than at other times, consistent with
365 the ratio of N_{CCN} (Fig. 2). This is consistent with there being a sizeable Twomey effect
366 associated with the contrast between periods of low and non-low CCN.

4. Back-trajectory and collocated satellite analysis

367 As described in section 2.3, three-dimensional Lagrangian back-trajectories are pro-
368 duced for each 6-hour period during the deployment. MODIS cloud LWP and N_d esti-
369 mates are associated with these trajectories (see section 2.4), and composites for low CCN
370 events and non-low CCN events are produced as a function of time prior to the trajec-
371 tory arrival at Graciosa. Because the Terra and Aqua overpass times are quite close, we
372 average trajectory-associated data from Terra and Aqua during the same day.

373 Before examining satellite composites, we first show trajectories ending at Graciosa
374 overlaid on MSLP maps at the start of all low CCN events (Fig. 12). Many, but not all,
375 of the events have a significant zonal (westerly) component, consistent with the evolution
376 of MSLP discussed in section 3.2 (Fig. 7). Many trajectories move off the North American
377 continent and pass over the Labrador sea area, and as many of these cases occur during
378 the winter and spring, one would expect many of them to be associated with cold air
379 outbreaks. This is indeed borne out with MCAO index (μ , Eqn 1) statistics. To assess
380 whether a given back-trajectory passes through a cold air outbreak region at some point,
381 we take the upper 90th percentile of μ along each trajectory, and then examine histograms

382 of this 90th percentile value for low CCN events and other cases. Taking simply the
383 maximum value produces similar results. Values of μ close to zero are indicative of cold
384 air outbreaks over water, and these are more than twice as commonly seen along low
385 CCN event back trajectories than in other cases (Fig. 13). Not all low CCN event back
386 trajectories are associated with cold air outbreaks, and so it is important to not overstate
387 the importance of cold air outbreaks, yet there is an interesting association that warrants
388 closer inspection.

389 The composite evolution of N_d for air masses reaching Graciosa during low CCN events
390 is contrasted with the behavior for non-low CCN cases (Fig. 14), showing that the N_d
391 distributions during low CCN events differ quite strongly in the few days running up to
392 the trajectory arrival at Graciosa (rightmost green bars in Fig. 14). Lower N_d values are
393 expected during low CCN events because previous observations have demonstrated that
394 N_d in the MBL is limited by CCN availability, particularly under low CCN conditions
395 [e.g., *Martin et al.*, 1994; *Ramanathan*, 2001; *Hudson et al.*, 2010; *Painemal and Zuidema*,
396 2013]. In the non-low CCN trajectory ensemble, the 50th percentile of N_d values in the
397 24-hour period prior to arrival at Graciosa is 50 cm^{-3} , but it is 25 cm^{-3} for the low CCN
398 cases, with each N_d distribution shifted to lower values. What is perhaps surprising is
399 that these differences in the N_d distributions are in place up to 4 days prior to arrival
400 at Graciosa. Prior to 4 days, the distributions become more alike and are statistically
401 indistinguishable. In other words, the divergence in N_d distributions begins several days
402 prior to arrival at Graciosa. This finding generally supports the idea that the processes
403 controlling the formation of low CCN events are generally not local to Graciosa, but appear
404 to be set in play by events occurring several days earlier. It is also interesting to note that

405 the time evolution of N_d over the 4 days prior to arrival shows that N_d is decreasing for
406 both low CCN event trajectories and non-low CCN cases (Fig. 14), suggesting that there
407 is a general reduction of N_d regardless of whether a trajectory becomes a low CCN event
408 or not. We discuss this further in section 5.

409 To gain further insight into the divergence of N_d distributions for low CCN events over
410 the days prior to arrival at Graciosa, Fig. 15 shows the corresponding time evolution of
411 cloud LWP (for liquid clouds) along the trajectories. Consistent with there being little
412 difference in LWP distributions observed at Graciosa between low CCN and non-low CCN
413 events (Fig. 9), the MODIS-derived LWP values in the 24 hours prior to trajectory arrival
414 at Graciosa also show little difference (Fig. 15). However, 2-4 days before arrival, LWPs
415 for low CCN events tend to be $\sim 30\%$ greater than those for non-low CCN cases. These
416 high LWP values occur as the relative divergence in N_d distributions ($[\text{non-low minus}$
417 $\text{low}]/\text{non-low}$) is increasing from ~ 0.3 to >0.4 (Fig. 14).

418 Examination of the individual back-trajectories reveals that several low CCN event tra-
419 jectories are associated with either marine or continental cold air outbreaks (Fig. 12). An
420 example of such a case can be seen in Fig. 16. This particular event encapsulates several
421 of the typical features seen for low CCN events determined in previous sections. First,
422 the trajectory shows southerly flow as the air mass reaches the Graciosa (right panels),
423 consistent with surface wind data (Fig. 6). Second, a low pressure center is located to the
424 west of Graciosa at this time, consistent with the average behavior for low CCN events
425 (Fig. 7). The low pressure cyclonic system results in a turning of the winds to southerly
426 during the final few hours prior to arrival at Graciosa. Prior to this, the trajectory spends
427 four days moving from the north and west (see central column in Fig. 16) as part of a

428 cold air outbreak emerging over the Labrador Sea between Greenland and Canada, as
429 indicated by the MCAO index (section 2.2), which is positive (left and center columns in
430 Fig. 16). Between 13 and 15 December, i.e., 2-4 days prior to arrival at Graciosa, the
431 cloud field at the trajectory location changes from overcast shallow stratocumulus clouds
432 that extend over a broad region to the east of Labrador to open mesoscale cellular convec-
433 tion. Observations and modeling have shown that transitions from closed to open cellular
434 convection in the Tropics/Subtropics are driven by strong drizzle that reaches the surface
435 [Mechem and Kogan, 2003; Stevens et al., 2005; Savic-Jovicic and Stevens, 2008; Wang
436 and Feingold, 2009] and are associated with large depletions of CCN through coalescence
437 scavenging [Sharon et al., 2006; Terai et al., 2014; Wang et al., 2010; Wood et al., 2011;
438 Berner et al., 2013]. In midlatitude cold air outbreaks, similarly high LWP and low N_d
439 are found [Field et al., 2014], suggesting that similar processes may be working to deplete
440 CCN.

5. Mechanisms for CCN Depletion

441 Based on the various observations presented above, it is clear that an explanation of
442 the mechanisms behind low CCN events at Graciosa requires understanding the evolution
443 of the boundary layer aerosol budget in air masses over several days prior to arriving at
444 the island. In this section, we explore possible mechanisms to help explain the low CCN
445 events. Quantifying terms in the CCN budget is challenging because of the complexity of
446 aerosol sources and sinks in the MBL [Fitzgerald, 1991; O'Dowd et al., 1997; Quinn and
447 Bates, 2011; Hudson et al., 2015]. Nevertheless, we are able to use observations here to
448 estimate some of the key source and sink terms.

5.1. Aerosol sinks

449 CCN in the MBL are lost through precipitation processes and through dry deposition,
450 the latter of which has been shown to be generally much smaller than the former [*Wood*
451 *et al.*, 2012]. In the cloudy MBL, and especially during the transition from closed to
452 open mesoscale cellular convection, coalescence scavenging is the dominant CCN sink
453 [*Berner et al.*, 2013]. We focus first on the shift in the N_d distributions to lower values
454 several days upstream of Graciosa (Fig. 14), and ask if this divergence can be caused
455 by the higher values of LWP at that time. We focus on the period 48-96 hours prior
456 to trajectory arrival at Graciosa and use the expression for loss rates discussed above in
457 the introduction that relates MBL-averaged CCN loss rates to cloud thickness [Eqn. 18
458 in *Wood*, 2006]. Assuming an adiabatic relationship between cloud thickness and LWP
459 [*Albrecht et al.*, 1990], we use a cloud top temperature of 275 K and pressure of 850 hPa to
460 estimate the adiabatic increase of LWC with altitude in cloud. We also assume an MBL
461 depth of 1500 m consistent with mean values over midlatitude oceans [*Rémillard et al.*,
462 2012; *Chan and Wood*, 2013]. The low CCN trajectory set has a median LWP (MODIS)
463 that is approximately 20-30% higher than that for non-low CCN cases (Fig. 15), but the
464 more skewed LWP distribution to higher values may also be important. To address this,
465 we use the entire LWP distribution in Fig. 15 for 48-96 hours prior to arrival at Graciosa
466 to estimate the mean MBL CCN loss rates, and find that for the low CCN trajectory set
467 the mean loss rate is $55 \text{ cm}^{-3} \text{ day}^{-1}$ compared to $35 \text{ cm}^{-3} \text{ day}^{-1}$ for the non-low CCN
468 set. Loss rates for other composite trajectory days are not markedly different for low and
469 non-low CCN events and are in the range $30\text{-}40 \text{ cm}^{-3} \text{ day}^{-1}$.

470 Assuming that the difference of $\sim 20 \text{ cm}^{-3} \text{ day}^{-1}$ in the mean loss rates for low and
471 non-low CCN trajectories is applicable to the entire two day period, and that source rates
472 are similar for the two trajectory sets, we can estimate that it would cause the mean N_d
473 values for the low CCN event trajectories to be reduced by several tens cm^{-3} compared
474 with the non-low CCN trajectories. Indeed, Fig. 14 does show that a differential of this
475 magnitude is evident in the N_d distributions during and after this period. Although
476 this calculation is not definitive, it does hint at possible cause of removal of CCN from
477 coalescence scavenging in anomalously thick liquid clouds that are associated with cold air
478 outbreaks.

5.2. Aerosol sources

479 Two of the main aerosol sources in the MBL are (a) particles derived from the ocean and
480 (b) entrainment of particles from the free troposphere [*Capaldo et al.*, 1999; *Katoshevski*
481 *et al.*, 1999; *Clarke et al.*, 2006; *Wood et al.*, 2012; *Clarke et al.*, 2013]. New particle
482 formation in the MBL is thought to be less important overall, although there appear to
483 be occasions where it does occur [*Tomlinson et al.*, 2007], and modeling work suggests
484 the possibility of new particle formation constituting a significant source of CCN during
485 conditions of ultralow CCN [*Kazil et al.*, 2011] in pockets of open cells. We have no
486 means to estimate the rate of new CCN production from new particle formation, but sea-
487 spray particle formation is wind speed dependent and can be estimated using previously
488 published formulations. Aqueous phase cloud processing within the MBL can also grow
489 particles, decreasing their critical supersaturation and effectively serving as a source of
490 CCN at low S [e.g., *Hudson et al.*, 2015], but the rate at which this occurs is contingent

491 on the availability of sulfate (and possibly organic) sources and is difficult to model in a
492 simple framework.

493 The entrainment rate of air from the free troposphere (FT) depends upon many fac-
494 tors [see e.g., *Wood, 2012; Clarke et al., 2013*]. An estimate of entrainment rate can be
495 made using energy, moisture and mass budgets [e.g., *Caldwell et al., 2005*], but satellite
496 observations show that over broad areas of the subtropical and tropical ocean the mean
497 entrainment rate only exceeds the mean subsidence rate by $\sim 30\%$ [*Wood and Bretherton,*
498 *2004*], so reanalysis estimates of subsidence rate should yield an estimate of the entrain-
499 ment rate better than a factor of two, and this approach was used in *Wood et al. [2012]*
500 to successfully predict N_d gradients over the southeastern Pacific. We make the same
501 assumption here to estimate mean entrainment rate for the trajectory groups. Mean sub-
502 sidence rates along the low CCN and non low CCN trajectories are found to be similar
503 (not shown) and are 2.0-2.5 mm s⁻¹. More uncertain is the concentration of CCN-sized
504 particles in the FT. In the Subtropical and Tropical regions, there is sufficient residence
505 time in the FT from new particle formation in the deep-convective detrainment regions
506 of the upper troposphere to allow the establishment of quasi self-preserving aerosol dis-
507 tributions, and this may limit the spatial and temporal variability of the aerosol size
508 distribution by the time parcels reach the lower FT [*Raes, 1995*]. In the midlatitudes,
509 however, the sources of FT particles are not as well quantified or understood. Summer-
510 time FT N_{CCN} at $S=0.2\%$, measured in the vicinity of the Azores are close to 100 cm⁻³
511 [*Hudson and Xie, 1999*], which is similar to FT values over the remote southeastern Pa-
512 cific [*Allen et al., 2011*], with values at S 0.1% expected to be slightly lower than this.
513 Such values are higher than MBL CCN concentrations at Graciosa during low CCN events

(Fig. 2), but similar to concentrations at other times, implying that entrainment from the FT is likely weakly buffering CCN losses from coalescence scavenging. Calculations of the replenishment rate from entrainment [see e.g., *Wood et al.*, 2012] indicate an upper limit for the buffering of CCN from FT entrainment of approximately $10\text{-}15\text{ cm}^{-3}\text{ day}^{-1}$ in the case that the MBL contains no CCN at all. In actual fact, mean CCN and N_d for both low CCN events and non-low cases (e.g., Fig. 14) are well above zero, so we estimate mean replenishment rates from entrainment to be $5\text{-}10\text{ cm}^{-3}\text{ day}^{-1}$ for low CCN events and $<5\text{ cm}^{-3}\text{ day}^{-1}$ for non-low CCN cases.

The other key aerosol source in the PBL is from sea-spray production, which is surface wind speed dependent. We use the approach taken in *Wood et al.* [2012] to estimate surface sea-spray production rates based on *Clarke et al.* [2006] and surface wind speeds taken from reanalysis data interpolated in time and space onto the HYSPLIT back-trajectories. CCN fluxes at $S=0.1\%$ are estimated assuming that emitted particles are sodium chloride. Based on this, we obtain a CCN flux rate equal to $\dot{N}_{\text{CCN},0.1\%} = Fu_{10}^{3.41}/z_i$ where u_{10} is the wind speed at an altitude of 10 m, z_i is the PBL depth, and F is an S -dependent function. Based on Fig. 1 in *Wood et al.* [2012], $F = 132\text{ m}^{-3}(\text{m s}^{-1})^{-2.41}$. As before, we assume $z_i=1500\text{ m}$, so that $\dot{N}_{\text{CCN},0.1\%} \approx 2, 20$ and $80\text{ cm}^{-3}\text{ day}^{-1}$ for $u_{10}=5, 10$ and 15 m s^{-1} respectively. As with the loss rates, we use the pdf of surface wind speeds along the trajectories to estimate mean CCN sea spray source rates. During the period 48-96 hr prior to arrival at Graciosa, the mean surface values of $\dot{N}_{\text{CCN},0.1\%}$ are estimated to be $15\text{-}20\text{ cm}^{-3}\text{ day}^{-1}$ with very little difference between rates for low CCN and non-low trajectories. A key implication of this is that differences in aerosol sources are not likely

536 to be responsible for the the differential in N_{CCN} (and N_d) between low CCN events and
537 non-low CCN cases.

5.3. Implications for overall CCN budget

538 For non-low CCN events, the calculations in the previous two subsections for the time
539 period 48-96 hrs prior to air mass arrival at Graciosa suggest surface sea-spray sources of
540 $15\text{-}20\text{ cm}^{-3}\text{ day}^{-1}$, with the mean source rate from FT entrainment of $<5\text{ cm}^{-3}\text{ day}^{-1}$, and
541 precipitation losses of $\sim 35\text{ cm}^{-3}\text{ day}^{-1}$. Assuming these are the primary terms in the CCN
542 budget, it is reasonable to expect that there would be a slow decline ($\sim 10\text{-}15\text{ cm}^{-3}\text{ day}^{-1}$)
543 in N_{CCN} and N_d over this period. Indeed, this is supported by observations (Fig. 14),
544 where median N_d falls by $\approx 25\text{ cm}^{-3}$ from 96 to 48 hours before arrival. For the low CCN
545 events, sea-spray source rates are estimated to be similar to those for non-low CCN cases
546 ($15\text{-}20\text{ cm}^{-3}\text{ day}^{-1}$), but the sink rate is closer to $55\text{ cm}^{-3}\text{ day}^{-1}$, and the FT aerosol
547 source is likely to be $\sim 5\text{-}10\text{ cm}^{-3}\text{ day}^{-1}$ because of the greater differential between the
548 concentration in the FT and the MBL. Thus, for low CCN events during 48-96 hrs prior
549 to arrival, we might expect mean overall CCN loss rates of perhaps $25\text{-}35\text{ cm}^{-3}\text{ day}^{-1}$, or
550 approximately double those for non-low CCN cases. Thus, we postulate that low CCN
551 events are driven by stronger coalescence scavenging in high LWP clouds associated with
552 cold air outbreaks $\sim 2\text{-}4$ days upstream of Graciosa.

6. Conceptual model

553 In this paper, we have identified a connection between cold air outbreak events and
554 subsequent very low CCN concentrations at Graciosa. Not all low CCN events can be
555 explained in this way, but a significant number of them can, and so we present Fig. 17

556 as a canonical case and as a means to introduce a conceptual model to explain how
557 low N_{CCN} in cold air outbreaks are created. Essentially, a deep surface low over the
558 northern North Atlantic (see left panels in Fig. 16) moves cold continental and/or polar
559 maritime air from the north and west over the warmer surface waters of the North Atlantic.
560 The strong surface fluxes encountered as the cold air streams over warmer waters result
561 initially in overcast stratocumulus clouds in a shallow PBL. Strong surface-driving and
562 also cloud-top longwave cooling helps drive turbulent entrainment that rapidly deepens
563 the PBL, resulting in cloud thickening and corresponding LWP increases. In the case
564 shown in Fig. 17, there is a large region over which the LWP exceeds 500 g m^{-2} , which
565 would remove CCN through coalescence scavenging at a rate of roughly $500 \text{ cm}^{-3} \text{ day}^{-1}$
566 according to the model used in section 5.1. In the trajectory ensemble mean, loss rates
567 via coalescence scavenging are clearly lower than this, but we demonstrate that the mean
568 loss rates are considerably higher for low CCN events because these trajectories encounter
569 clouds with higher LWP. The conceptual model encapsulated in Fig. 17, and particularly
570 the spatial extent of the cold air outbreak open cell clouds, suggests that basin-scale CCN
571 variability may be induced by cold air outbreaks, and that more attention should be paid
572 to the causes of CCN variability in the midlatitude marine PBL.

7. Conclusions

573 In this study, we examine aerosol, cloud and meteorological characteristics of very low
574 CCN events (6 hour mean N_{CCN} at $S = 0.1\%$ below 20 cm^{-3}) occurring at Graciosa
575 Island in the eastern North Atlantic. The various findings from this study were used to
576 propose a conceptual model to explain the occurrence of very low N_{CCN} in the remote
577 MBL. Table 2 summarizes the key meteorological aspects that differentiate low CCN

578 events from non-low CCN conditions. The association of a number of the low CCN events
579 with cold air outbreak conditions upstream is particularly interesting and important, and
580 examining the seasonality of cold air outbreak events may help to explain the apparent
581 seasonal preference for low CCN events during winter and spring. *Kolstad et al.* [2009]
582 examined the seasonal cycle of the MCAO index (Eqn. 1) over a broad region of the NW
583 Atlantic including the Labrador Sea over which a number of the low CCN event trajectories
584 passed, and found maximum values from December to March, with the seasonality largely
585 driven by colder 700 hPa temperatures during these months. Our analysis of the MCAO
586 index along the back-trajectories arriving at Graciosa (Fig. 13) shows that low CCN
587 event back-trajectories are approximately twice as likely to have encountered a cold air
588 outbreak compared to other cases.

589 We find that N_d are lower at Graciosa during low CCN events than at other times, but
590 that the reductions in N_d that lead to these differences happen several days upstream of
591 Graciosa, often during cold air outbreaks, where coincident LWP values are anomalously
592 large. Based on this, it is hypothesized here that coalescence scavenging of cloud droplets
593 during precipitation formation under high LWP conditions associated with cold air out-
594 breaks may be partly responsible for the shift of the low CCN event N_d distribution to
595 smaller values in trajectories that constitute low CCN events. We hope that our findings
596 and conceptual model can inform further study of factors controlling aerosol variability
597 at the Azores and over the remote subtropical and midlatitude oceans in general.

8. Acknowledgements

598 The CAP-MBL deployment of the ARM Mobile Facility was supported by the U.S.
599 Department of Energy (DOE) Atmospheric Radiation Measurement (ARM) Program Cli-

600 mate Research Facility and the DOE Atmospheric Sciences Program. We are indebted to
601 the scientists and staff who made this work possible by taking and quality-controlling the
602 measurements. Data were obtained from the ARM program archive, sponsored by DOE,
603 Office of Science, Office of Biological and Environmental Research Environmental Science
604 Division. This work was supported by DOE Grants DE SC0006865MOD0002 and DE-
605 SC0013489 [PI Robert Wood]. MODIS data were obtained from the NASA Goddard Land
606 Processes data archive, GOES data from the NOAA CLASS website, and SSM/I data from
607 Remote Sensing Systems (data from <http://www.remss.com>). ERA-Interim data are pro-
608 vided by the European Center for Medium Range Weather Forecasts (ECMWF). The
609 HYSPLIT IV model was obtained from the NOAA Air Resources Laboratory.

9. Appendix: Corrections to CCN counter

610 As mentioned in section 2.1.1, the CCN measurements were found to be problematic
611 for October 2009 to June 2010, and a flow-rate correction is described here that uses the
612 CN counter as a reference instrument. Köhler calculations indicate that a supersaturation
613 S of approximately 1% should be sufficient to activate most soluble particles larger than
614 20 nm in diameter. Remote marine regions away from sources of significant new par-
615 ticle formation, observations indicate relatively few particles in the size range 10-20 nm
616 [Heintzenberg *et al.*, 2000; Allen *et al.*, 2011]. Therefore, we would expect N_{CCN} measured
617 at $S \approx 1\%$ to be close to the concentrations from the CN counter. At the beginning of the
618 record (April-September 2009) and after the cleaning (July-December 2010), this is quite
619 close to what we observe, although the CN counter monthly mean concentrations tend to
620 be approximately 20% below those from the CCN counter at $S = 1.11\%$ (Fig. 1a). Other
621 than during the problematic period (Oct 2009-June 2010), the ratio of CN to CCN at

622 $S = 1.11\%$ is stable (compare periods before and after the degraded period in Fig. 1a),
623 suggesting that either the CCN counter or CN counter has a stable systematic bias in
624 measured concentration. In this study, we assume that the CN counter is correct, al-
625 though assuming the reverse has no significant impact upon the primary conclusions of
626 this study.

627 Importantly, we note that the degradation in concentrations from October 2009 to
628 June 2010 is seen in all channels (Fig. 1). The ratio of N_{CCN} measured at any two
629 supersaturations is stable and shows no sign of changing during the degradation period
630 (not shown). For example, the ratio of N_{CCN} at 0.1% to that at 1.11% is 0.19 (with
631 the month to month standard deviation of this ratio of 0.04) during the months of good
632 counter operation, and 0.17 (s.d. 0.04) during the degraded months. This indicates that
633 the degradation is affecting concentrations at all S in the same way, and that a single
634 sample volume correction for one S can be applied to all S . We apply this correction on
635 a monthly basis by multiplying the monthly mean CCN at $S = 1.11\%$ to ensure equality
636 with the monthly mean N_{CN} (with high variance measurements removed as discussed
637 in the caption for (Fig. 1). The monthly multiplication factors are then applied to
638 concentrations at all supersaturations during the month. Corrected N_{CCN} is shown in
639 Fig. 1b. Although we have no independent means to verify the accuracy of the corrected
640 concentrations, we note that the seasonal cycle of submicron aerosol scattering coefficient
641 at 450 nm wavelength tracks quite well the concentrations of particles at the lower S
642 (Fig. 1b). Corrected N_{CCN} are used exclusively in this study.

References

- 643 Albrecht, B. A., C. W. Fairall, D. W. Thomson, A. B. White, J. B. Snider, and W. H.
644 Schubert (1990), Surface-based remote sensing of the observed and the Adiabatic liq-
645 uid water content of stratocumulus clouds, *Geophys. Res. Lett.*, *17*(1), 89–92, doi:
646 10.1029/GL017i001p00089.
- 647 Allen, G., H. Coe, A. Clarke, C. Bretherton, R. Wood, S. J. Abel, P. Barrett,
648 P. Brown, R. George, S. Freitag, C. McNaughton, S. Howell, L. Shank, V. Kapustin,
649 V. Brekhovskikh, L. Kleinman, Y.-N. Lee, S. Springston, T. Toniazzo, R. Krejci,
650 J. Fochesatto, G. Shaw, P. Krecl, B. Brooks, G. McMeeking, K. N. Bower, P. I. Williams,
651 J. Crosier, I. Crawford, P. Connolly, J. D. Allan, D. Covert, A. R. Bandy, L. M. Russell,
652 J. Trembath, M. Bart, J. B. McQuaid, J. Wang, and D. Chand (2011), South East Pa-
653 cific atmospheric composition and variability sampled along 20 S during VOCALS-REx,
654 *Atmospheric Chemistry and Physics*, *11*(11), 5237–5262, doi:10.5194/acp-11-5237-2011.
- 655 Andreae, M. O. (2007), Aerosols Before Pollution, *Science*, *315*(5808), 50–51, doi:
656 10.1126/science.1136529.
- 657 Baker, M. B., and R. J. Charlson (1990), Bistability of CCN concentrations and ther-
658 modynamics in the cloud-topped boundary layer, *Nature*, *345*(6271), 142–145, doi:
659 10.1038/345142a0.
- 660 Bennartz, R. (2007), Global assessment of marine boundary layer cloud droplet num-
661 ber concentration from satellite, *Journal of Geophysical Research*, *112*(D2), doi:
662 10.1029/2006JD007547.
- 663 Berner, A. H., C. S. Bretherton, R. Wood, and A. Muhlbauer (2013), Marine boundary
664 layer cloud regimes and POC formation in a CRM coupled to a bulk aerosol scheme,

665 *Atmospheric Chemistry and Physics*, 13(24), 12,549–12,572, doi:10.5194/acp-13-12549-
666 2013.

667 Boers, R., and R. M. Mitchell (1994), Absorption feedback in stratocumulus clouds
668 Influence on cloud top albedo, *Tellus A*, 46(3), 229–241, doi:10.1034/j.1600-
669 0870.1994.00001.x.

670 Boers, R., J. B. Jensen, and P. B. Krummel (1998), Microphysical and short-wave radia-
671 tive structure of stratocumulus clouds over the Southern Ocean: Summer results and
672 seasonal differences, *Quarterly Journal of the Royal Meteorological Society*, 124(545),
673 151–168.

674 Boers, R., J. R. Acarreta, and J. L. Gras (2006), Satellite monitoring of the first indi-
675 rect aerosol effect: Retrieval of the droplet concentration of water clouds, *Journal of*
676 *Geophysical Research*, 111(D22), doi:10.1029/2005JD006838.

677 Caldwell, P., C. S. Bretherton, and R. Wood (2005), Mixed-layer budget analysis of
678 the diurnal cycle of entrainment in southeast Pacific stratocumulus., *Journal of the*
679 *atmospheric sciences*, 62(10).

680 Capaldo, K. P., P. Kasibhatla, and S. N. Pandis (1999), Is aerosol production within
681 the remote marine boundary layer sufficient to maintain observed concentrations?, *J.*
682 *Geophys. Res.*, 104(D3), 3483–3500, doi:10.1029/1998JD100080.

683 Carslaw, K. S., L. A. Lee, C. L. Reddington, K. J. Pringle, A. Rap, P. M. Forster, G. W.
684 Mann, D. V. Spracklen, M. T. Woodhouse, L. A. Regayre, and J. R. Pierce (2013), Large
685 contribution of natural aerosols to uncertainty in indirect forcing, *Nature*, 503(7474),
686 67–71, doi:10.1038/nature12674.

687 Chan, K. M., and R. Wood (2013), The seasonal cycle of planetary boundary layer
688 depth determined using COSMIC radio occultation data: SEASONAL CYCLE OF
689 PBL DEPTH, *Journal of Geophysical Research: Atmospheres*, 118(22), 12,422–12,434,
690 doi:10.1002/2013JD020147.

691 Clarke, A. D., S. R. Owens, and J. Zhou (2006), An ultrafine sea-salt flux from breaking
692 waves: Implications for cloud condensation nuclei in the remote marine atmosphere,
693 *JGR*, 111(D6), doi:10.1029/2005JD006565.

694 Clarke, A. D., S. Freitag, R. M. C. Simpson, J. G. Hudson, S. G. Howell, V. L.
695 Brekhovskikh, T. Campos, V. N. Kapustin, and J. Zhou (2013), Free troposphere as a
696 major source of CCN for the equatorial pacific boundary layer: long-range transport
697 and teleconnections, *Atmos. Chem. Phys.*, 13(15), 7511–7529, doi:10.5194/acp-13-7511-
698 2013.

699 Comstock, K. K., R. Wood, S. E. Yuter, and C. S. Bretherton (2004), Reflectivity and rain
700 rate in and below drizzling stratocumulus, *Quarterly Journal of the Royal Meteorological*
701 *Society*, 130(603), 2891–2918, doi:10.1256/qj.03.187.

702 Dee, D. P., S. M. Uppala, A. J. Simmons, P. Berrisford, P. Poli, S. Kobayashi, U. Andrae,
703 M. A. Balmaseda, G. Balsamo, P. Bauer, P. Bechtold, A. C. M. Beljaars, L. van de Berg,
704 J. Bidlot, N. Bormann, C. Delsol, R. Dragani, M. Fuentes, A. J. Geer, L. Haimberger,
705 S. B. Healy, H. Hersbach, E. V. Hlm, L. Isaksen, P. Kllberg, M. Khler, M. Matricardi,
706 A. P. McNally, B. M. Monge-Sanz, J.-J. Morcrette, B.-K. Park, C. Peubey, P. de Ros-
707 nay, C. Tavalato, J.-N. Thpaut, and F. Vitart (2011), The ERA-Interim reanalysis:
708 configuration and performance of the data assimilation system, *Q.J.R. Meteorol. Soc.*,
709 137(656), 553–597, doi:10.1002/qj.828.

- 710 Draxier, R., and G. Hess (1998), An overview of the HYSPLIT_4 modelling system for
711 trajectories, dispersion and deposition, *AUSTRALIAN METEOROLOGICAL MAGA-*
712 *ZINE*, *47*(4), 295–308.
- 713 Feingold, G., S. M. Kreidenweis, B. Stevens, and W. R. Cotton (1996), Numerical sim-
714 ulations of stratocumulus processing of cloud condensation nuclei through collision-
715 coalescence, *J. Geophys. Res.*, *101*(D16), 21,391–21,402, doi:10.1029/96JD01552.
- 716 Field, P. R., R. J. Cotton, K. McBeath, A. P. Lock, S. Webster, and R. P. Allan (2014),
717 Improving a convection-permitting model simulation of a cold air outbreak: Simula-
718 tion of a Cold Air Outbreak, *Quarterly Journal of the Royal Meteorological Society*,
719 *140*(678), 124–138, doi:10.1002/qj.2116.
- 720 Fitzgerald, J. W. (1991), Marine aerosols: A review, *Atmospheric Environment. Part A.*
721 *General Topics*, *25*(34), 533–545, doi:10.1016/0960-1686(91)90050-H.
- 722 Ghan, S. J., S. J. Smith, M. Wang, K. Zhang, K. Pringle, K. Carslaw, J. Pierce, S. Bauer,
723 and P. Adams (2013), A simple model of global aerosol indirect effects: GLOBAL
724 AEROSOL INDIRECT EFFECTS, *Journal of Geophysical Research: Atmospheres*,
725 *118*(12), 6688–6707, doi:10.1002/jgrd.50567.
- 726 Goren, T., and D. Rosenfeld (2015), Extensive closed cell marine stratocumulus downwind
727 of EuropeA large aerosol cloud mediated radiative effect or forcing?, *J. Geophys. Res.*
728 *Atmos.*, p. 2015JD023176, doi:10.1002/2015JD023176.
- 729 Grosvenor, D. P., and R. Wood (2014), The effect of solar zenith angle on MODIS cloud
730 optical and microphysical retrievals within marine liquid water clouds, *ACP*, *14*(14),
731 7291–7321, doi:10.5194/acp-14-7291-2014.

- 732 Hamilton, D. S., L. A. Lee, K. J. Pringle, C. L. Reddington, D. V. Spracklen, and
733 K. S. Carslaw (2014), Occurrence of pristine aerosol environments on a polluted planet,
734 *PNAS*, *111*(52), 18,466–18,471, doi:10.1073/pnas.1415440111.
- 735 Heintzenberg, J., D. C. Covert, and R. Van Dingenen (2000), Size distribution and chem-
736 ical composition of marine aerosols: a compilation and review, *Tellus B*, *52*(4), 1104–
737 1122.
- 738 Hindman, E. E., W. M. Porch, J. G. Hudson, and P. A. Durkee (1994), Ship-produced
739 cloud lines of 13 July 1991, *Atmospheric Environment*, *28*(20), 3393–3403, doi:
740 10.1016/1352-2310(94)00171-G.
- 741 Hudson, J. G., and S. Noble (2009), CCN and cloud droplet concentrations at a remote
742 ocean site, *Geophysical Research Letters*, *36*(13), doi:10.1029/2009GL038465.
- 743 Hudson, J. G., and Y. Xie (1999), Vertical distributions of cloud condensation nuclei
744 spectra over the summertime northeast Pacific and Atlantic Oceans, *J. Geophys. Res.*,
745 *104*(D23), 30,219–30,229, doi:10.1029/1999JD900413.
- 746 Hudson, J. G., S. Noble, and V. Jha (2010), Stratus cloud supersaturations: STRATUS
747 CLOUD SUPERSATURATIONS, *Geophysical Research Letters*, *37*(21), n/a–n/a, doi:
748 10.1029/2010GL045197.
- 749 Hudson, J. G., S. Noble, and S. Tabor (2015), Cloud supersaturations from CCN
750 spectra Hoppel minima, *J. Geophys. Res. Atmos.*, *120*(8), 2014JD022,669, doi:
751 10.1002/2014JD022669.
- 752 IPCC (2013), *Summary for Policymakers*, book section SPM, p. 130, Cambridge
753 University Press, Cambridge, United Kingdom and New York, NY, USA, doi:
754 10.1017/CBO9781107415324.004.

- 755 Isaksen, I. S. A., C. Granier, G. Myhre, T. K. Berntsen, S. B. Dalsren, M. Gauss,
756 Z. Klimont, R. Benestad, P. Bousquet, W. Collins, T. Cox, V. Eyring, D. Fowler,
757 S. Fuzzi, P. Jckel, P. Laj, U. Lohmann, M. Maione, P. Monks, A. S. H. Prevot, F. Raes,
758 A. Richter, B. Rognerud, M. Schulz, D. Shindell, D. S. Stevenson, T. Storelvmo, W. C.
759 Wang, M. van Weele, M. Wild, and D. Wuebbles (2009), Atmospheric composition
760 change: ClimateChemistry interactions, *Atmospheric Environment*, *43*(33), 5138–5192,
761 doi:10.1016/j.atmosenv.2009.08.003.
- 762 Jefferson, A. (2010), Empirical estimates of CCN from aerosol optical properties at four
763 remote sites, *Atmospheric Chemistry and Physics*, *10*(14), 6855–6861, doi:10.5194/acp-
764 10-6855-2010.
- 765 Kalnay, E., M. Kanamitsu, R. Kistler, W. Collins, D. Deaven, L. Gandin, M. Iredell,
766 S. Saha, G. White, J. Woollen, Y. Zhu, A. Leetmaa, R. Reynolds, M. Chelliah,
767 W. Ebisuzaki, W. Higgins, J. Janowiak, K. C. Mo, C. Ropelewski, J. Wang, R. Jenne,
768 and D. Joseph (1996), The NCEP/NCAR 40-Year Reanalysis Project, *Bull. Amer.*
769 *Meteor. Soc.*, *77*(3), 437–471, doi:10.1175/1520-0477(1996)077<0437:TNYRP>2.0.CO;2.
- 770 Katoshevski, D., A. Nenes, and J. H. Seinfeld (1999), A STUDY OF PROCESSES THAT
771 GOVERN THE MAINTENANCE OF AEROSOLS IN THE MARINE BOUNDARY
772 LAYER, *Journal of Aerosol Science*, *30*(4), 503–532, doi:10.1016/S0021-8502(98)00740-
773 X.
- 774 Kazil, J., H. Wang, G. Feingold, A. D. Clarke, J. R. Snider, and A. R. Bandy (2011),
775 Modeling chemical and aerosol processes in the transition from closed to open cells
776 during VOCALS-REx, *Atmos. Chem. Phys.*, *11*(15), 7491–7514, doi:10.5194/acp-11-
777 7491-2011.

- 778 King, M. D., S.-C. Tsay, S. E. Platnick, M. Wang, and K.-N. Liou (1997), Cloud retrieval
779 algorithms for modis: Optical thickness, effective particle radius, and thermodynamic
780 phase, *MODIS Algorithm Theoretical Basis Document ATBD-MOD-05*, NASA.
- 781 Kolstad, E. W., and T. J. Bracegirdle (2007), Marine cold-air outbreaks in the future: an
782 assessment of IPCC AR4 model results for the Northern Hemisphere, *ClimDyn*, *30*(7-8),
783 871–885, doi:10.1007/s00382-007-0331-0.
- 784 Kolstad, E. W., T. J. Bracegirdle, and I. A. Seierstad (2009), Marine cold-air outbreaks in
785 the North Atlantic: temporal distribution and associations with large-scale atmospheric
786 circulation, *ClimDyn*, *33*(2-3), 187–197, doi:10.1007/s00382-008-0431-5.
- 787 Lance, S., A. Nenes, J. Medina, and J. N. Smith (2006), Mapping the Operation of the
788 DMT Continuous Flow CCN Counter, *Aerosol Science and Technology*, *40*(4), 242–254,
789 doi:10.1080/02786820500543290.
- 790 Lewis, E. R., and S. E. Schwartz (2004), *Sea salt aerosol production: mechanisms, meth-*
791 *ods, measurements, and models – A critical review.*
- 792 Martin, G. M., D. W. Johnson, and A. Spice (1994), The Measurement and Parameteri-
793 zation of Effective Radius of Droplets in Warm Stratocumulus Clouds, *J. Atmos. Sci.*,
794 *51*(13), 1823–1842, doi:10.1175/1520-0469(1994)051<1823:TMAPOE>2.0.CO;2.
- 795 Mauritsen, T., J. Sedlar, M. Tjernström, C. Leck, M. Martin, M. Shupe, S. Sjogren,
796 B. Sierau, P. O. G. Persson, I. M. Brooks, and E. Swietlicki (2011), An Arctic CCN-
797 limited cloud-aerosol regime, *Atmos. Chem. Phys.*, *11*(1), 165–173, doi:10.5194/acp-11-
798 165-2011.
- 799 McComiskey, A., G. Feingold, A. S. Frisch, D. D. Turner, M. A. Miller, J. C. Chiu,
800 Q. Min, and J. A. Ogren (2009), An assessment of aerosol-cloud interactions in marine

801 stratus clouds based on surface remote sensing, *J. Geophys. Res.*, *114*(D9), D09,203,
802 doi:10.1029/2008JD011006.

803 Mechem, D. B., and Y. L. Kogan (2003), Simulating the Transition from Drizzling Marine
804 Stratocumulus to Boundary Layer Cumulus with a Mesoscale Model, *Mon. Wea. Rev.*,
805 *131*(10), 2342–2360, doi:10.1175/1520-0493(2003)131;2342:STTFDM;2.0.CO;2.

806 Mechem, D. B., P. C. Robinson, and Y. L. Kogan (2006), Processing of cloud condensation
807 nuclei by collision-coalescence in a mesoscale model, *Journal of Geophysical Research*,
808 *111*(D18), doi:10.1029/2006JD007183.

809 Miles, N. L., J. Verlinde, and E. E. Clothiaux (2000), Cloud droplet size distributions in
810 low-level stratiform clouds, *Journal of the atmospheric sciences*, *57*(2), 295–311.

811 O’Dowd, C. D., M. H. Smith, I. E. Consterdine, and J. A. Lowe (1997), Marine aerosol,
812 sea-salt, and the marine sulphur cycle: a short review, *Atmospheric Environment*, *31*(1),
813 73–80, doi:10.1016/S1352-2310(96)00106-9.

814 Oreopoulos, L. (2005), The impact of subsampling on MODIS level-3 statistics of cloud
815 optical thickness and effective radius, *IEEE Transactions on Geoscience and Remote*
816 *Sensing*, *43*(2), 366–373, doi:10.1109/TGRS.2004.841247.

817 Painemal, D., and P. Zuidema (2013), The first aerosol indirect effect quantified through
818 airborne remote sensing during VOCALS-REx, *Atmos. Chem. Phys.*, *13*(2), 917–931,
819 doi:10.5194/acp-13-917-2013.

820 Platnick, S., and S. Twomey (1994), Determining the Susceptibility of Cloud
821 Albedo to Changes in Droplet Concentration with the Advanced Very
822 High Resolution Radiometer, *JAppMet*, *33*(3), 334–347, doi:10.1175/1520-
823 0450(1994)033;0334:DTSOCA;2.0.CO;2.

- 824 Quinn, P. K., and T. S. Bates (2011), The case against climate regulation via oceanic
825 phytoplankton sulphur emissions, *Nature*, *480*(7375), 51–56, doi:10.1038/nature10580.
- 826 Raes, F. (1995), Entrainment of free tropospheric aerosols as a regulating mechanism
827 for cloud condensation nuclei in the remote marine boundary layer, *J. Geophys. Res.*,
828 *100*(D2), 2893–2903, doi:10.1029/94JD02832.
- 829 Ramanathan, V. (2001), Aerosols, Climate, and the Hydrological Cycle, *Science*,
830 *294*(5549), 2119–2124, doi:10.1126/science.1064034.
- 831 Rémillard, J., P. Kollias, E. Luke, and R. Wood (2012), Marine Boundary Layer Cloud
832 Observations in the Azores, *Journal of Climate*, *25*(21), 7381–7398, doi:10.1175/JCLI-
833 D-11-00610.1.
- 834 Riihimaki, L., S. McFarlane, and C. Sivaraman (2014), Droplet Number Concentrations
835 Value-Added Product, *US Department of Energy Report, DOE/SC-ARM-TR-140*, 29
836 pp.
- 837 Roberts, G. C., and A. Nenes (2005), A Continuous-Flow Streamwise Thermal-Gradient
838 CCN Chamber for Atmospheric Measurements, *Aerosol Science and Technology*, *39*(3),
839 206–221, doi:10.1080/027868290913988.
- 840 Savic-Jovicic, V., and B. Stevens (2008), The Structure and Mesoscale Organization of
841 Precipitating Stratocumulus, *Journal of the Atmospheric Sciences*, *65*(5), 1587–1605,
842 doi:10.1175/2007JAS2456.1.
- 843 Sharon, T. M., B. A. Albrecht, H. H. Jonsson, P. Minnis, M. M. Khaiyer, T. M. van Reken,
844 J. Seinfeld, and R. Flagan (2006), Aerosol and cloud microphysical characteristics of rifts
845 and gradients in maritime stratocumulus clouds, *Journal of the atmospheric sciences*,
846 *63*(3), 983–997.

- 847 Shinozuka, Y., A. D. Clarke, A. Nenes, A. Jefferson, R. Wood, C. S. McNaughton, J. Strm,
848 P. Tunved, J. Redemann, K. L. Thornhill, R. H. Moore, T. L. Latham, J. J. Lin, and
849 Y. J. Yoon (2015), The relationship between cloud condensation nuclei (CCN) con-
850 centration and light extinction of dried particles: indications of underlying aerosol pro-
851 cesses and implications for satellite-based CCN estimates, *Atmos. Chem. Phys. Discuss.*,
852 *15*(2), 2745–2789, doi:10.5194/acpd-15-2745-2015.
- 853 Stevens, B., G. Vali, K. Comstock, R. Wood, M. C. Van Zanten, P. H. Austin, C. S.
854 Bretherton, and D. H. Lenschow (2005), POCKETS OF OPEN CELLS AND DRIZZLE
855 IN MARINE STRATOCUMULUS, *Bulletin of the American Meteorological Society*,
856 *86*(1), 51–57, doi:10.1175/BAMS-86-1-51.
- 857 Terai, C. R., C. S. Bretherton, R. Wood, and G. Painter (2014), Aircraft observations
858 of aerosol, cloud, precipitation, and boundary layer properties in pockets of open cells
859 over the southeast Pacific, *Atmospheric Chemistry and Physics*, *14*(15), 8071–8088,
860 doi:10.5194/acp-14-8071-2014.
- 861 Tomlinson, J. M., R. Li, and D. R. Collins (2007), Physical and chemical properties of the
862 aerosol within the southeastern Pacific marine boundary layer, *Journal of Geophysical*
863 *Research*, *112*(D12), doi:10.1029/2006JD007771.
- 864 Turner, D., S. Clough, J. Liljegren, E. Clothiaux, K. Cady-Pereira, and K. Gaustad
865 (2007), Retrieving Liquid Water Path and Precipitable Water Vapor From the Atmo-
866 spheric Radiation Measurement (ARM) Microwave Radiometers, *IEEE Transactions on*
867 *Geoscience and Remote Sensing*, *45*(11), 3680–3690, doi:10.1109/TGRS.2007.903703.
- 868 Twomey, S., and T. A. Wojciechowski (1969), Observations of the Geographi-
869 cal Variation of Cloud Nuclei, *J. Atmos. Sci.*, *26*(4), 648–651, doi:10.1175/1520-

- 870 0469(1969)26;648:OOTGVO;2.0.CO;2.
- 871 VanZanten, M. C., B. Stevens, G. Vali, and D. H. Lenschow (2005), Observations of drizzle
872 in nocturnal marine stratocumulus, *Journal of the atmospheric sciences*, *62*(1), 88–106.
- 873 Wang, H., and G. Feingold (2009), Modeling Mesoscale Cellular Structures and Drizzle
874 in Marine Stratocumulus. Part II: The Microphysics and Dynamics of the Boundary
875 Region between Open and Closed Cells, *Journal of the Atmospheric Sciences*, *66*(11),
876 3257–3275, doi:10.1175/2009JAS3120.1.
- 877 Wang, H., G. Feingold, R. Wood, and J. Kazil (2010), Modelling microphysical and meteo-
878 rological controls on precipitation and cloud cellular structures in Southeast Pacific stra-
879 tocumulus, *Atmospheric Chemistry and Physics*, *10*(13), 6347–6362, doi:10.5194/acp-
880 10-6347-2010.
- 881 Wood, R. (2006), Rate of loss of cloud droplets by coalescence in warm clouds, *Journal*
882 *of Geophysical Research*, *111*(D21), doi:10.1029/2006JD007553.
- 883 Wood, R. (2012), Stratocumulus Clouds, *Monthly Weather Review*, *140*(8), 2373–2423,
884 doi:10.1175/MWR-D-11-00121.1.
- 885 Wood, R., and C. S. Bretherton (2004), Boundary layer depth, entrainment, and decou-
886 pling in the cloud-capped subtropical and tropical marine boundary layer., *Journal of*
887 *climate*, *17*(18).
- 888 Wood, R., C. S. Bretherton, D. Leon, A. D. Clarke, P. Zuidema, G. Allen, and H. Coe
889 (2011), An aircraft case study of the spatial transition from closed to open mesoscale
890 cellular convection over the Southeast Pacific, *Atmospheric Chemistry and Physics*,
891 *11*(5), 2341–2370, doi:10.5194/acp-11-2341-2011.

892 Wood, R., D. Leon, M. Lebsock, J. Snider, and A. D. Clarke (2012), Precipitation driv-
893 ing of droplet concentration variability in marine low clouds, *JGR-Atmos*, *117*(D19),
894 D19,210, doi:10.1029/2012JD018305.

895 Wood, R., M. Wyant, C. S. Bretherton, J. Rmillard, P. Kollias, J. Fletcher, J. Stemmler,
896 S. de Szoeke, S. Yuter, M. Miller, D. Mechem, G. Tselioudis, J. C. Chiu, J. A. L. Mann,
897 E. J. OConnor, R. J. Hogan, X. Dong, M. Miller, V. Ghate, A. Jefferson, Q. Min,
898 P. Minnis, R. Palikonda, B. Albrecht, E. Luke, C. Hannay, and Y. Lin (2015), Clouds,
899 Aerosols, and Precipitation in the Marine Boundary Layer: An Arm Mobile Facility De-
900 ployment, *Bull. Amer. Meteor. Soc.*, *96*(3), 419–440, doi:10.1175/BAMS-D-13-00180.1.

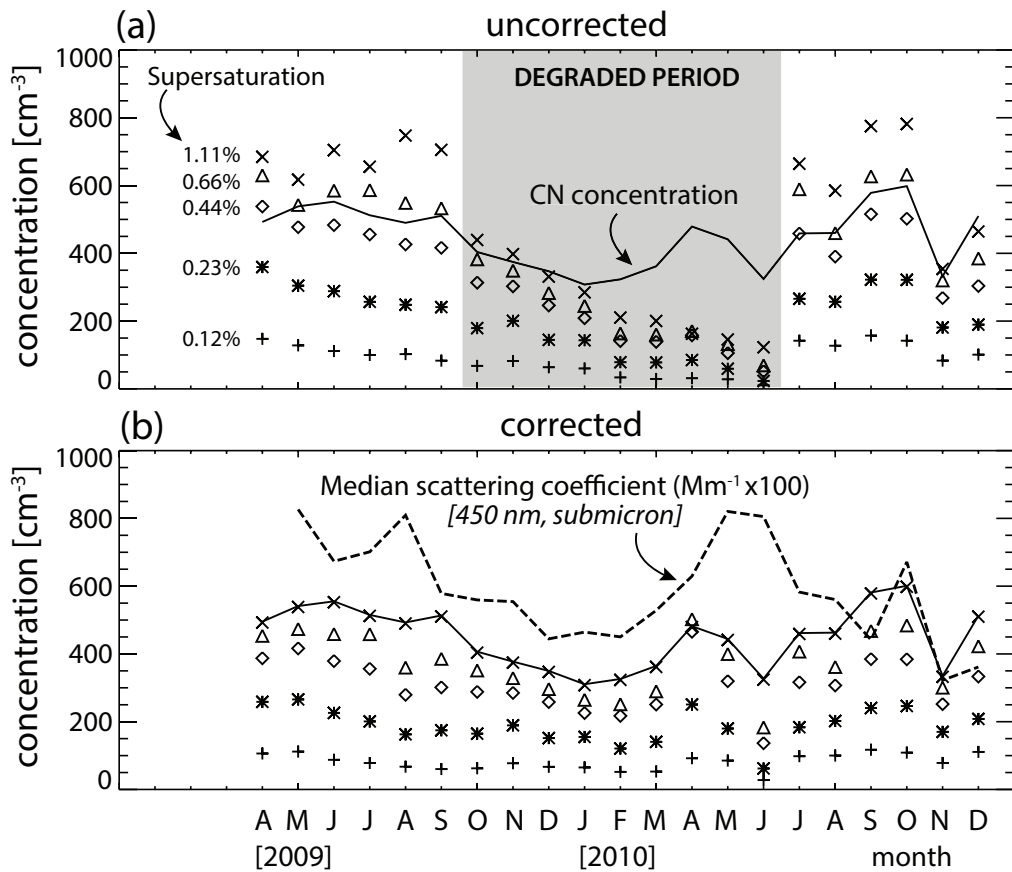


Figure 1. (a) Time series of monthly mean particle concentrations from the CCN counter (symbols), for five different supersaturations, with different symbols indicating different supersaturations listed in the upper panel immediately to the left of the symbols. Monthly mean N_{CN} is shown as the solid line. Prior to construction of monthly mean values, to avoid contamination by local pollution, individual measurements (typically 4 minutes for a CCN measurement at a single supersaturation) that have high concentration variance are screened out by removing cases where the relative standard deviation (standard deviation/mean) exceeds unity. The period where the CCN counter was degraded is shown in gray. (b) CCN concentrations after the correction procedure has been applied. N_{CN} is also shown as in panel (a). Also shown in panel (b) is a time series of the monthly median submicron blue (450 nm) aerosol scattering coefficient.

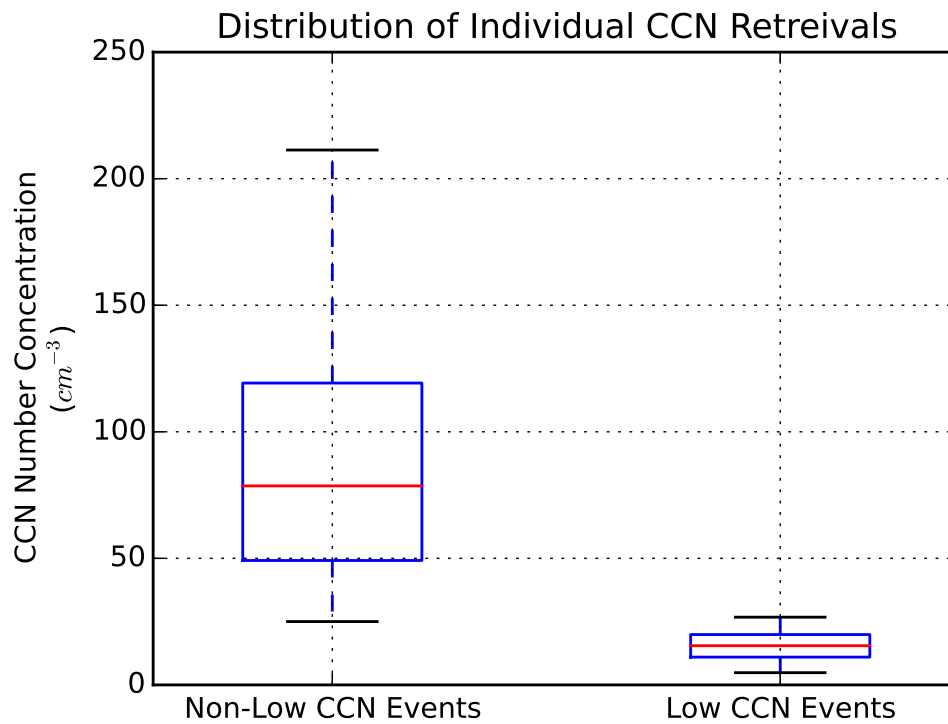


Figure 2. Box-whisker plots showing the distribution of all CCN measurements (not simply 6 hour means) at $S = 0.1\%$ for the non-low (left) and low CCN (right) events during the entire deployment. Boxes show 25th, 50th (red line) and 75th percentiles, and whiskers reach out to show the 5th and 95th percentiles.

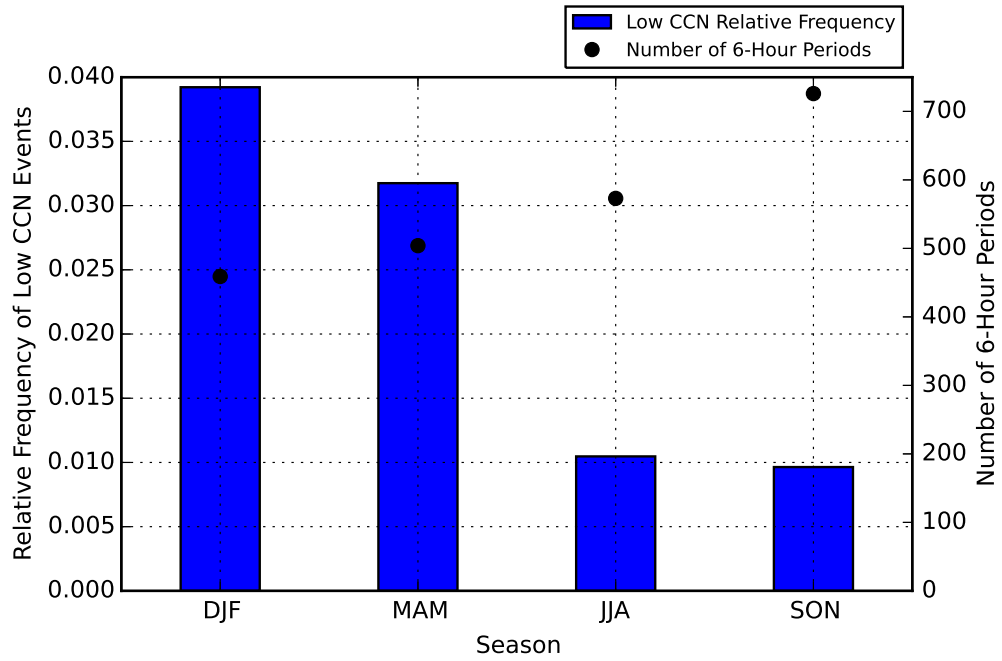


Figure 3. Winter and spring are the dominant seasons for low CCN events at Graciosa. Figure shows the frequency of occurrence of low CCN events (number of 6-hour events/number of available 6-hour periods) by season (blue bars, left axis) and the total number of 6 hour time periods of available data for each season (black circles, right axis).

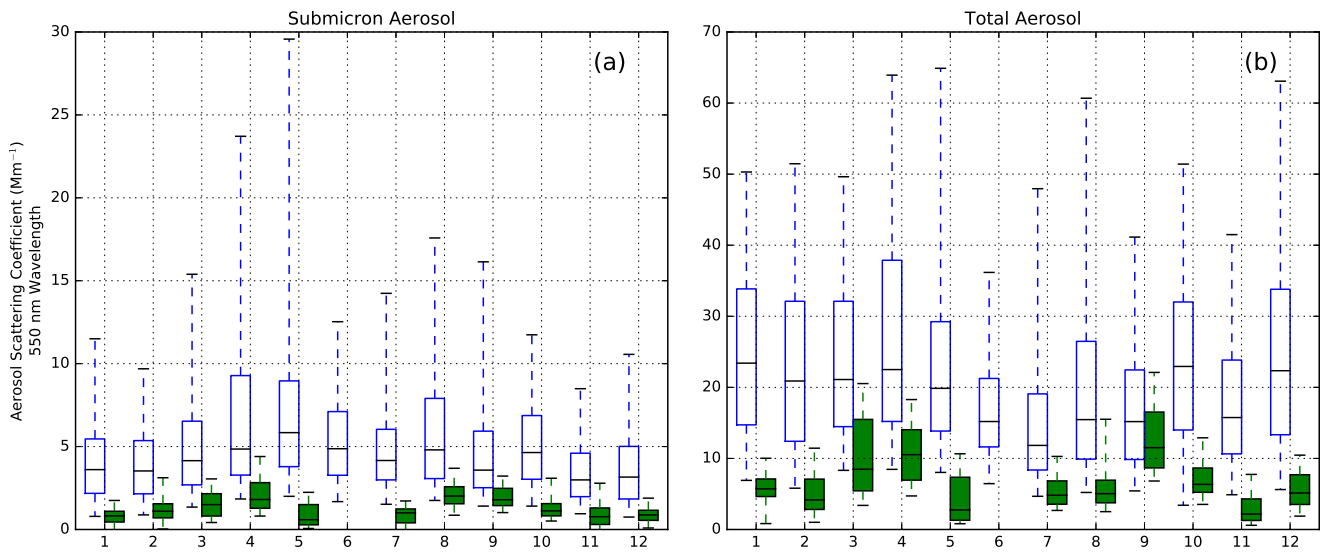


Figure 4. Aerosol scattering is reduced during low CCN cases both for submicron and sub- $10\mu\text{m}$ particles. Monthly mean climatology of (a) submicron and (b) total (sub- $10\mu\text{m}$) aerosol scattering coefficient at 550 nm wavelength for low CCN cases (green box-whiskers) and for non-low CCN cases (blue). Boxes show 25th, 50th (line) and 75th percentiles, and whiskers reach out to show the 5th and 95th percentiles.

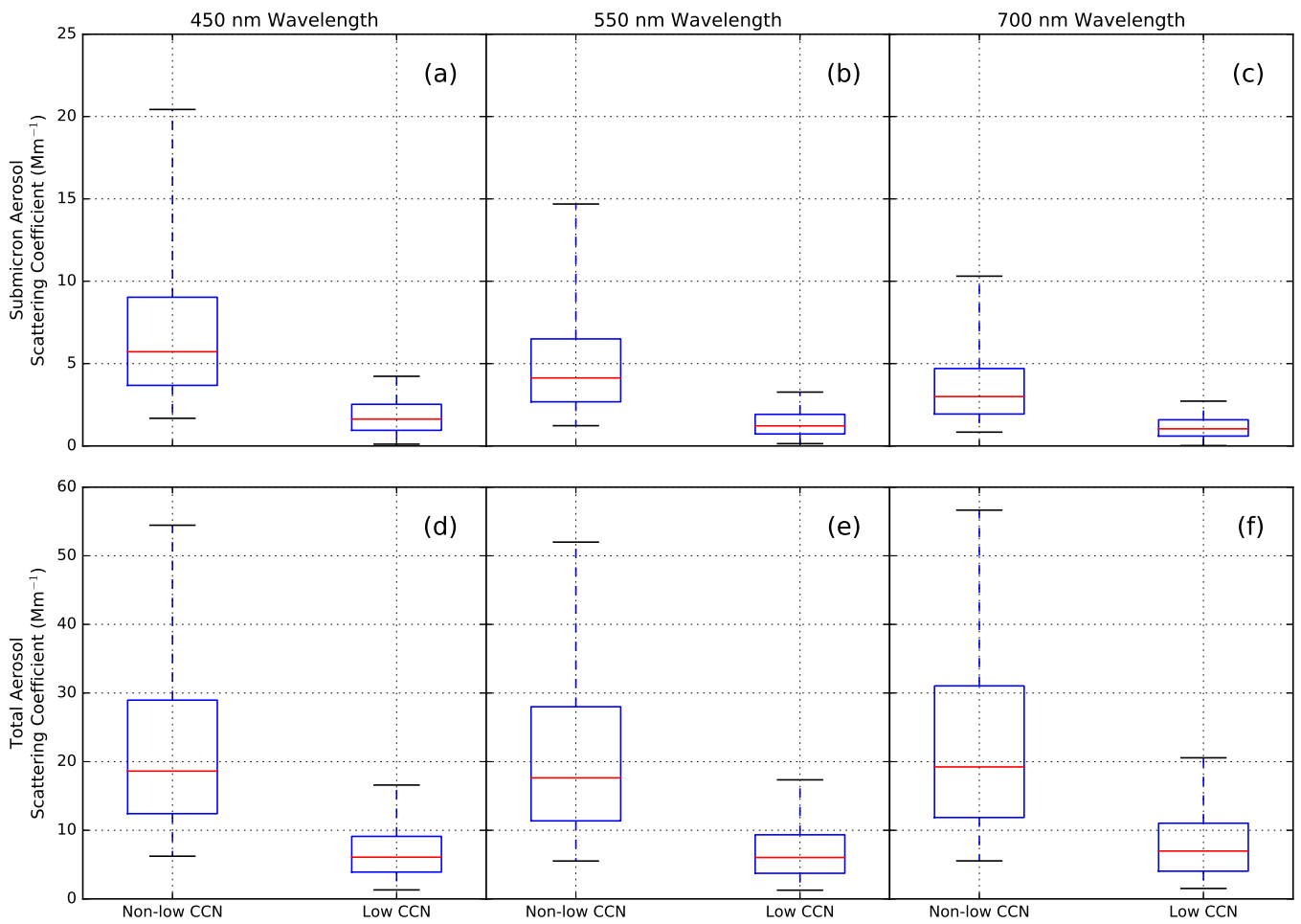


Figure 5. Aerosol scattering is reduced for low CCN at all wavelengths and for both submicron and sub- $10\mu\text{m}$ particles. Figure shows box-whisker histograms (see caption for Fig. 2) for low CCN events (right bars in each panel) and for non-low CCN events (left bars). The top row (panels a, b, c) is for submicron scattering and the bottom row (panels d, e, f) is for sub- $10\mu\text{m}$ scattering. Each column of panels shows a different wavelength: 450 nm (a, d), 550 nm (b, e) and 700 nm (c, f).

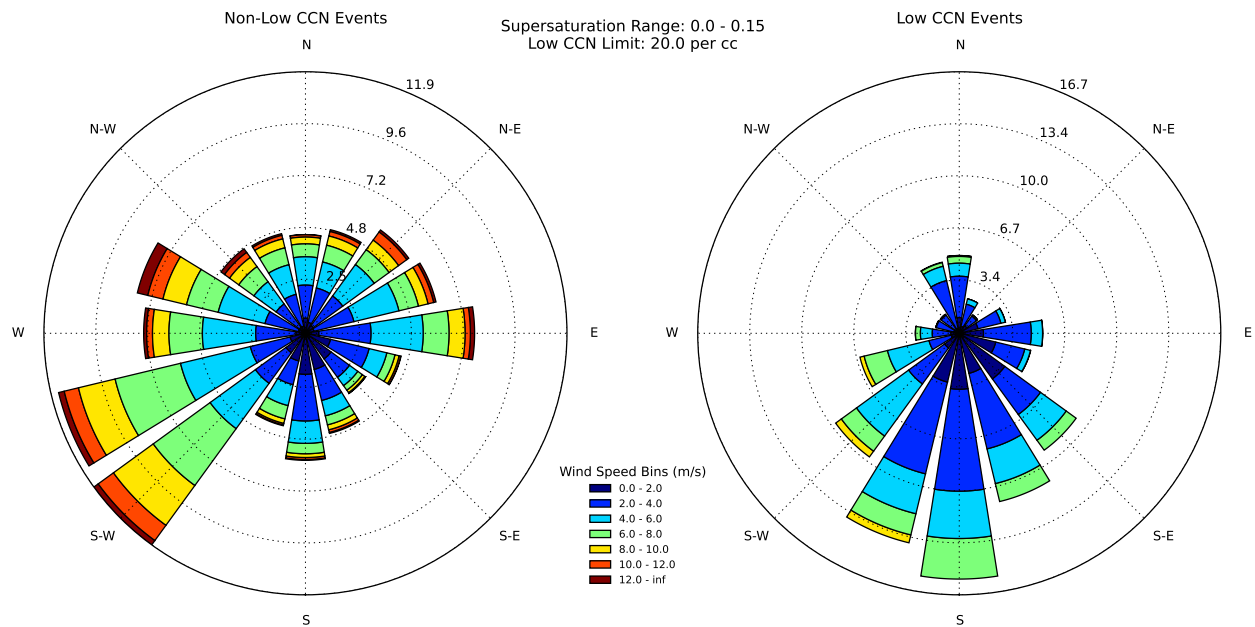


Figure 6. Low CCN cases tend to occur during conditions of weak southerly surface winds. Surface wind rose pdfs for (a) non-low CCN and (b) low CCN events. The length of the radial bars is the frequency of winds of a given direction, and the colors indicate the frequency of different wind speeds. The distribution of wind speed and direction is markedly different for the low CCN events.

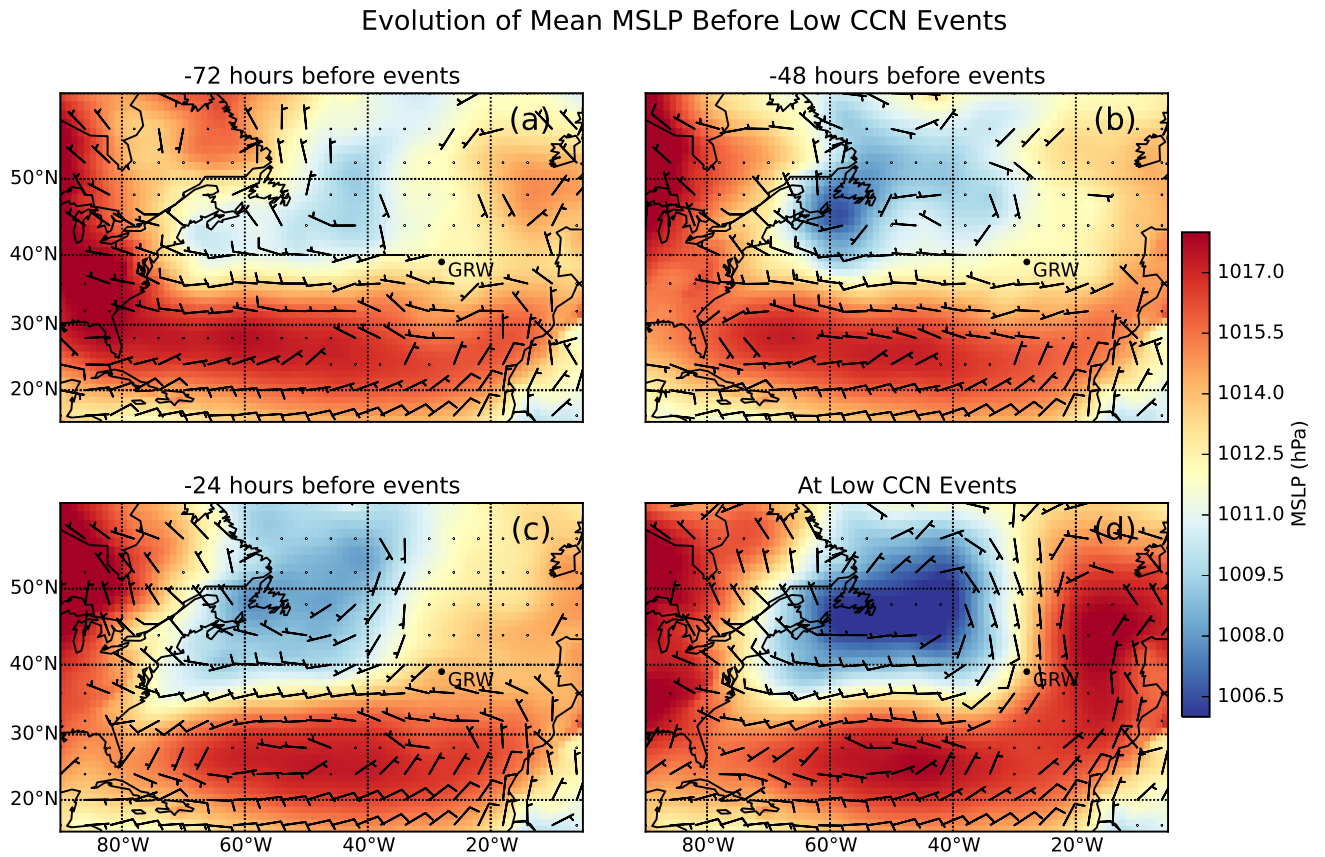


Figure 7. Composite mean sea-level pressure (MSLP) for low CCN events (a) 72 hours, (b) 48 hours, (c) 24 hours prior to, and (d) at the start of low CCN events at Graciosa. The location of Graciosa is marked as GRW. Mean barbs are also shown with mean wind speeds in knots (full barb=10 kt; half barb=5 kt).

Evolution of Mean MSLP Anomalies Before Low CCN Events

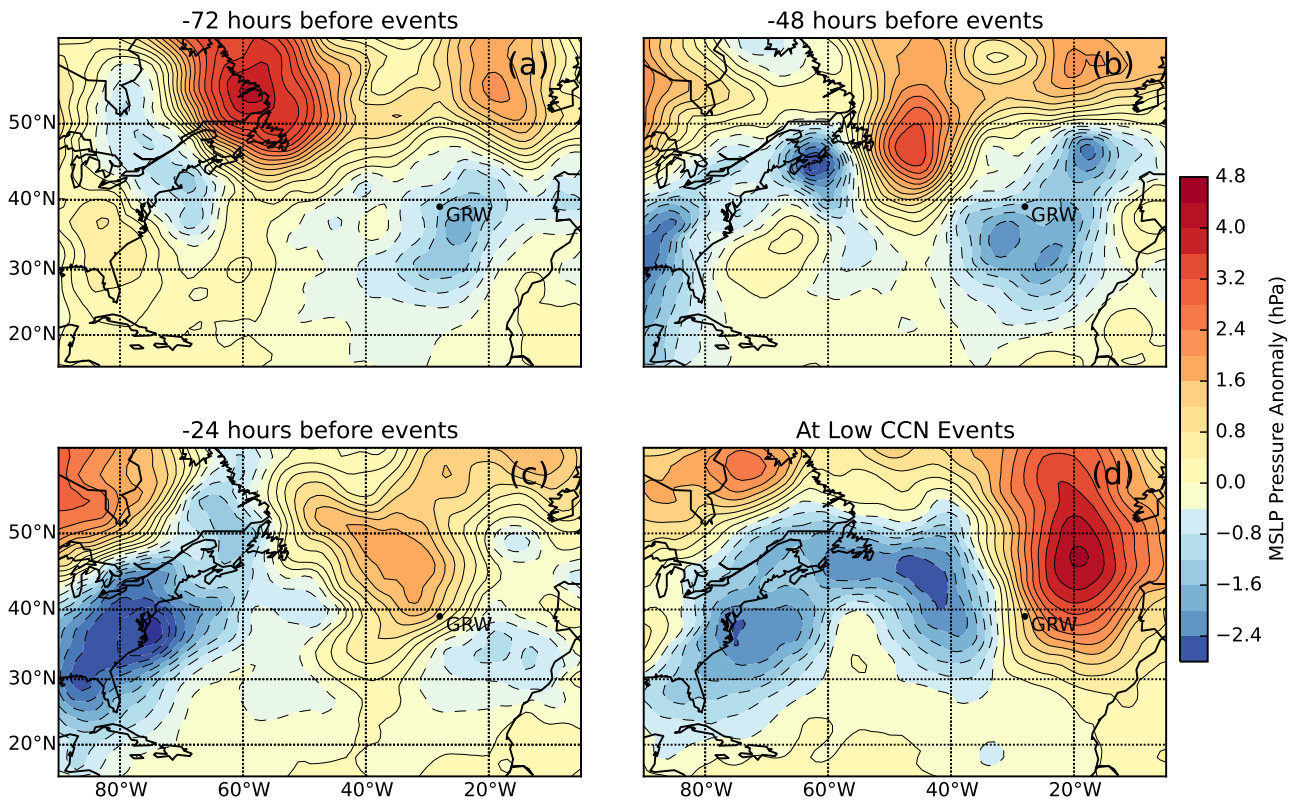


Figure 8. Composite difference in SLP anomalies (30 day running mean SLP removed) between low CCN events and non-low CCN cases. The panels show the anomalies (a) 72 hours, (b) 48 hours, and (c) 24 hours prior to the low CCN events at Graciosa, and (d) during the low CCN events. SLP fields for the low CCN cases are taken from the beginning of the 6 hour period of the event. The location of Graciosa is marked as GRW.

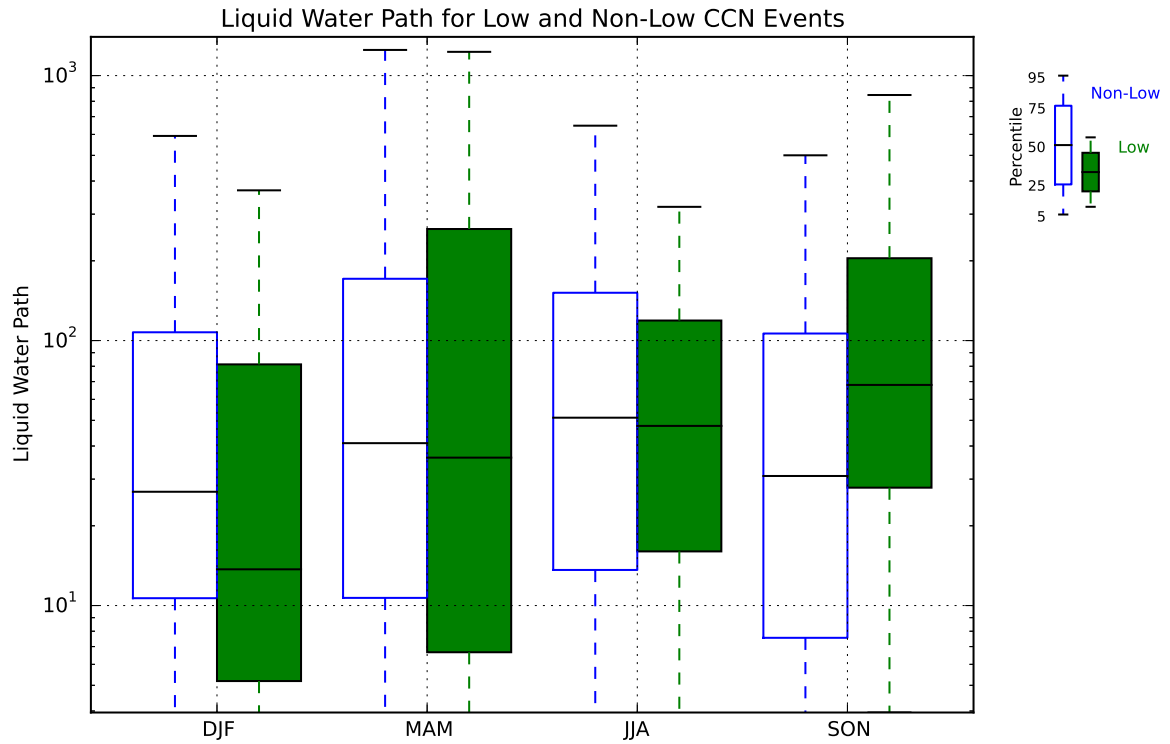


Figure 9. LWP distributions (units g m^{-2}) from the ground-based MWR at Graciosa for low CCN cases (solid green box-whiskers) and for non-low CCN cases (open blue box-whiskers), broken down by season.

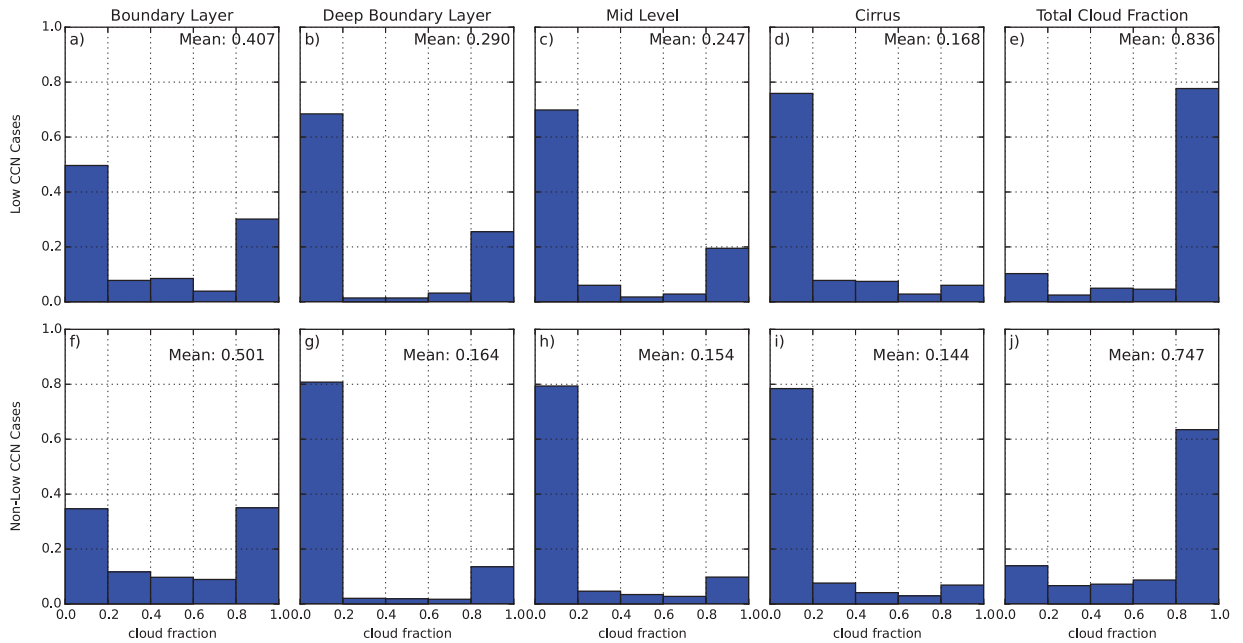


Figure 10. Cloud fraction histograms for different cloud types and total cloud fraction during low CCN events (panels a-e) and for non-low CCN cases (panels f-j). The cloud types are from *Rémillard et al.* [2012] and are described in section 2.1.2. Each panel also shows the fraction of each cloud type observed. Note that the sum of cloud fractions over each type is greater than the overall cloud fraction because more than one cloud type can be present at the same time.

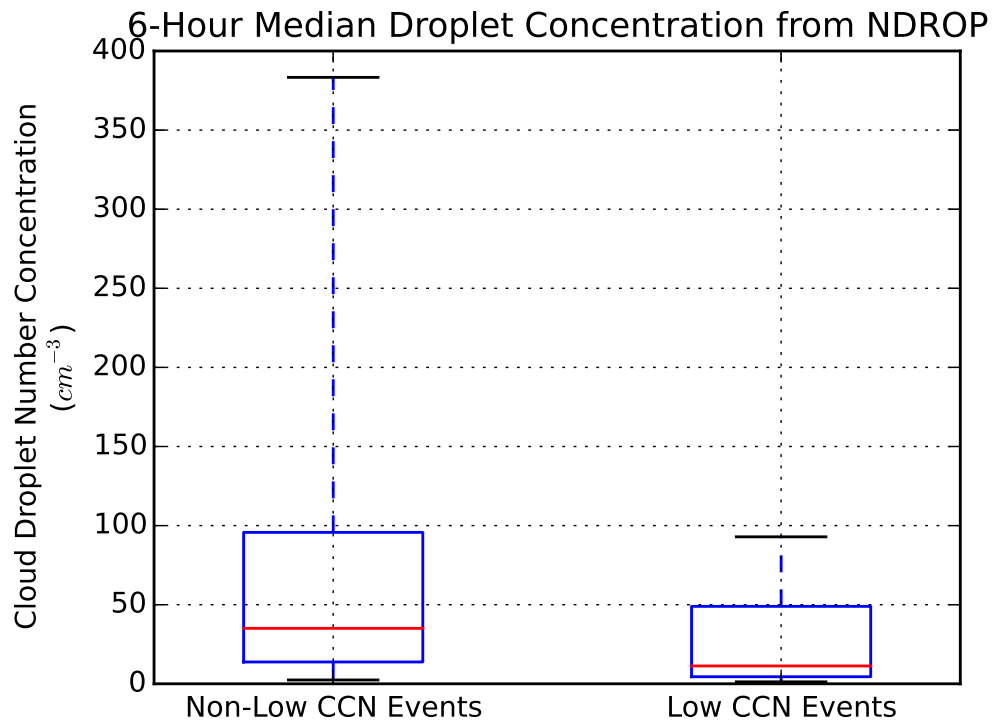


Figure 11. Box-whisker plots showing the distribution of 6-hour median surface-derived N_d measurements at Graciosa for the non-low (left) and low CCN (right) events during the entire deployment. Boxes show 25th, 50th (red line) and 75th percentiles, and whiskers reach out to show the 5th and 95th percentiles.

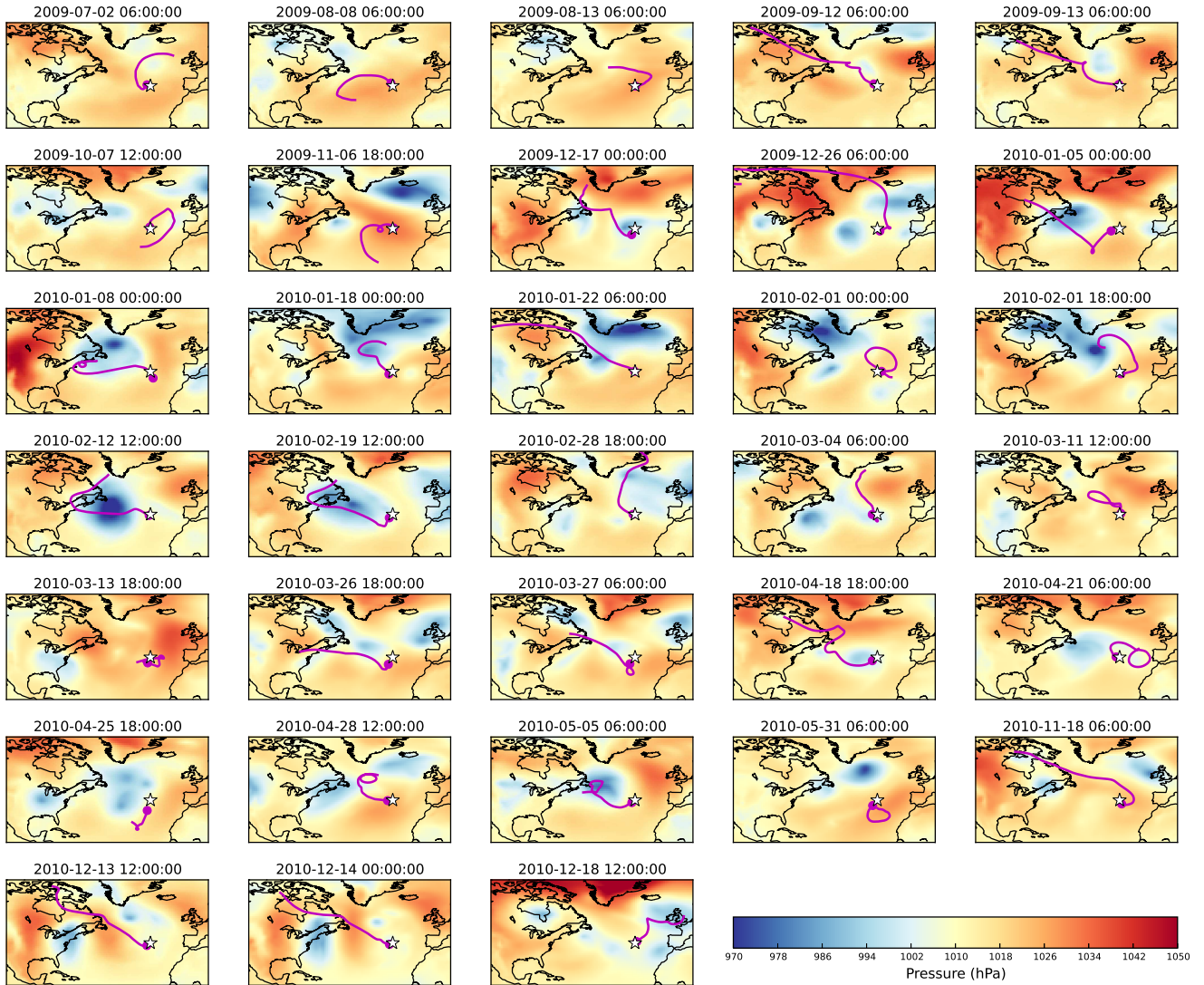


Figure 12. Maps of MSLP (colors) for all low CCN events at Graciosa (star) at the event start time, with their respective 148-hour back trajectories overlaid.

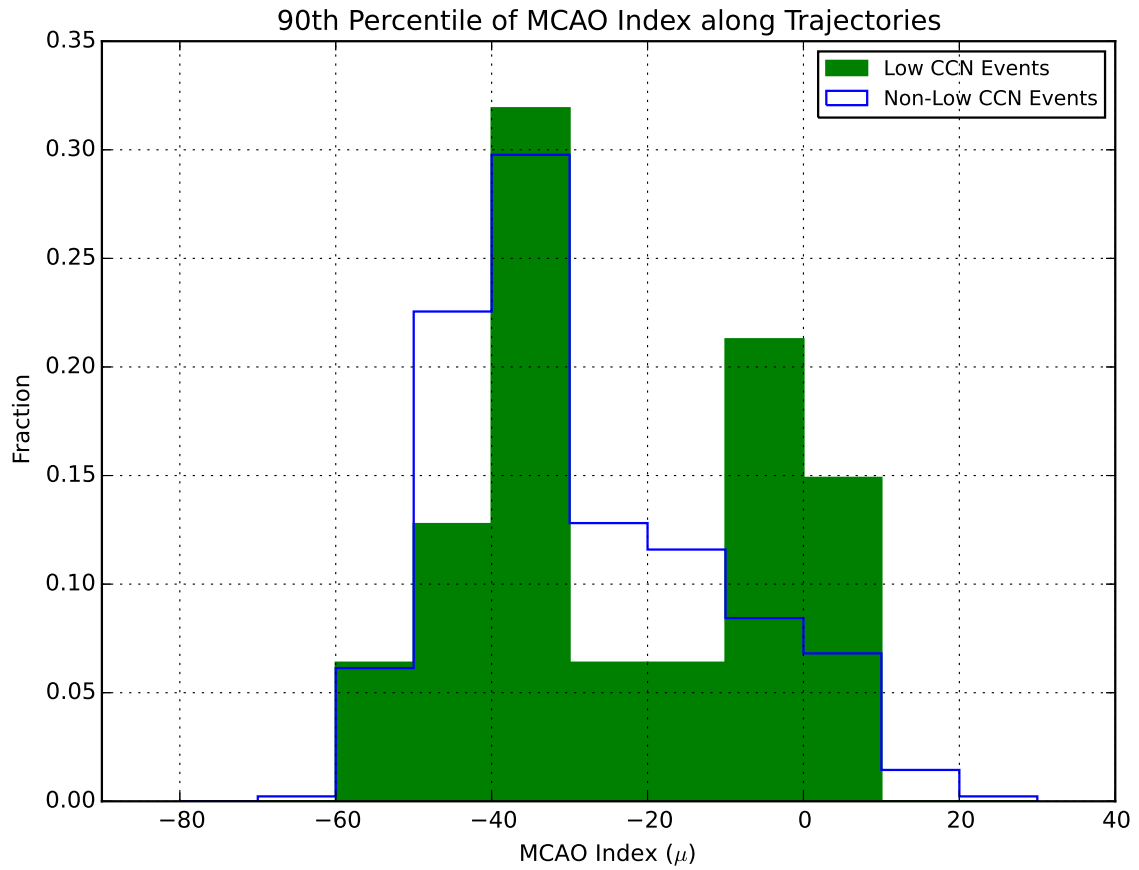


Figure 13. Trajectories resulting in low CCN events at Graciosa tend to have encountered cold air outbreaks more frequently. Figure shows histograms of the upper 90th percentile of the MCAO index (μ , see Eqn. 1) along each back trajectory, for low CCN cases (solid green) and for non-low CCN cases (open blue).

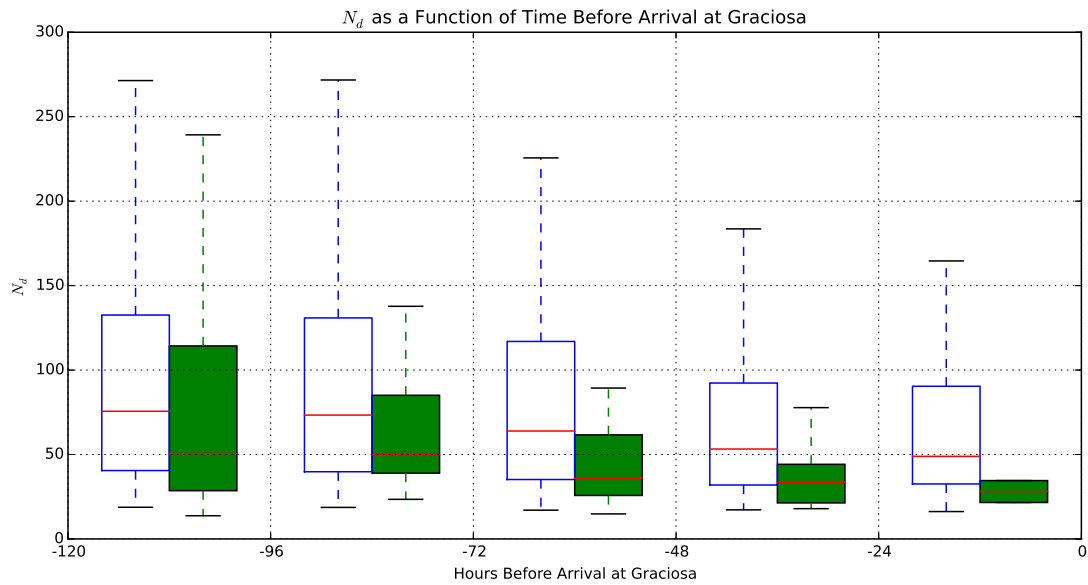


Figure 14. Composite behavior of MODIS-derived cloud droplet number concentration N_d taken from the ensemble of low CCN (solid green box-whiskers) and non-low CCN cases (open blue box-whiskers) as a function of time before reaching Graciosa. Box-whiskers show 25, 50, 75th percentiles (box) and 5/95th percentiles of N_d (whiskers) from all the collocated satellite overpasses crossing the back-trajectories. Fractional reductions of N_d for low CCN events compared with non-low CCN cases are 0.32, 0.33, 0.35, 0.40 and 0.46 respectively for the five days prior to arrival.

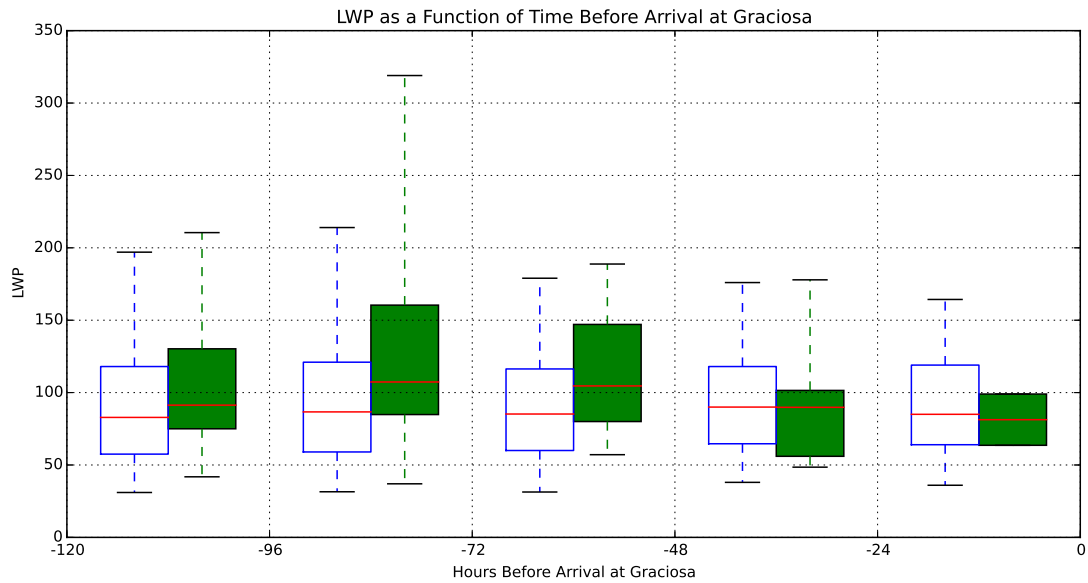


Figure 15. Composite behavior of MODIS-derived cloud LWP taken from the ensemble of low CCN (solid green box-whiskers) and non-low CCN cases (open blue box-whiskers) as a function of time before reaching Graciosa. Box-whiskers show 25, 50, 75th percentiles (box) and 5/95th percentiles of N_d (whiskers) from all the collocated satellite overpasses crossing the back-trajectories.

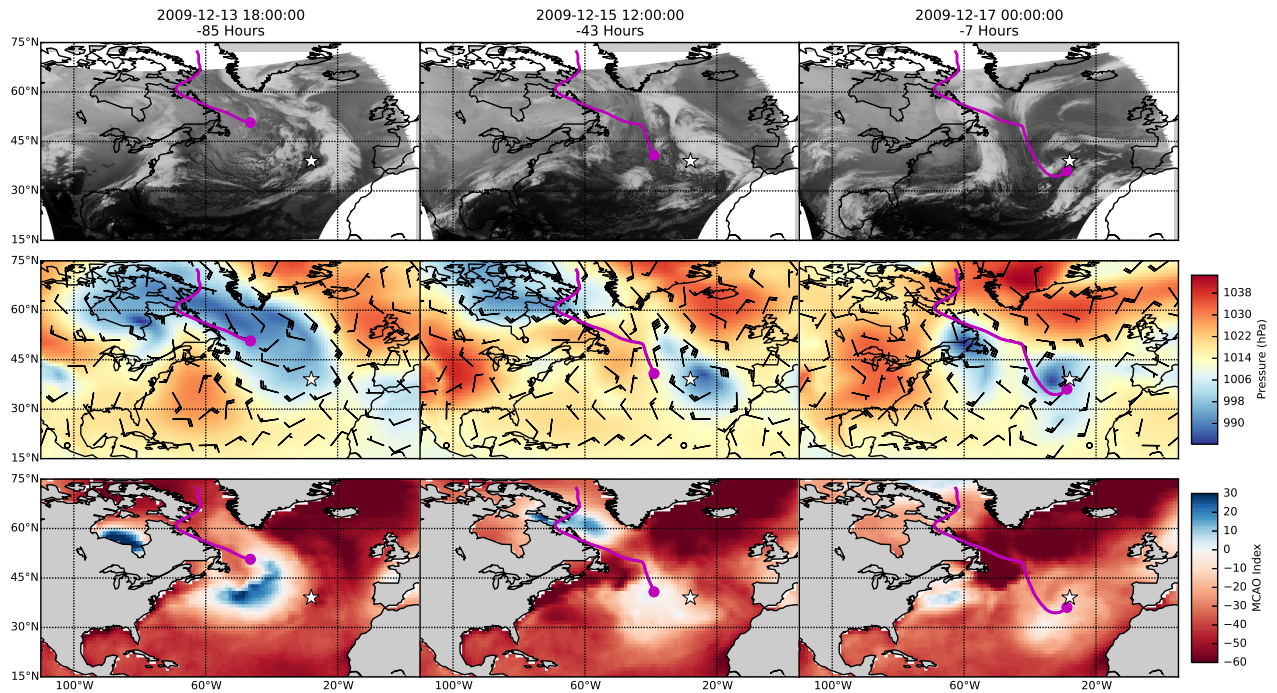


Figure 16. Evolution of cloud (top row, thermal infrared GOES imagery with light colors representing cold clouds), mean sea level pressure and wind barbs (center row, knots for wind speeds using standard meteorological convention) and a marine cold air outbreak (MCAO) index (bottom row, with values close to zero and above indicative of cold air outbreaks, see text) for a cold air outbreak case resulting in a low CCN event at Graciosa on 17 December 2009 that lasted from 00 UTC to 12 UTC. The left, center and right columns of panels show data at 85, 43 and 7 hours prior to trajectory arrival during the middle of the low CCN event at Graciosa. The trajectory is shown in each panel, with the circle at its end location at the corresponding time.

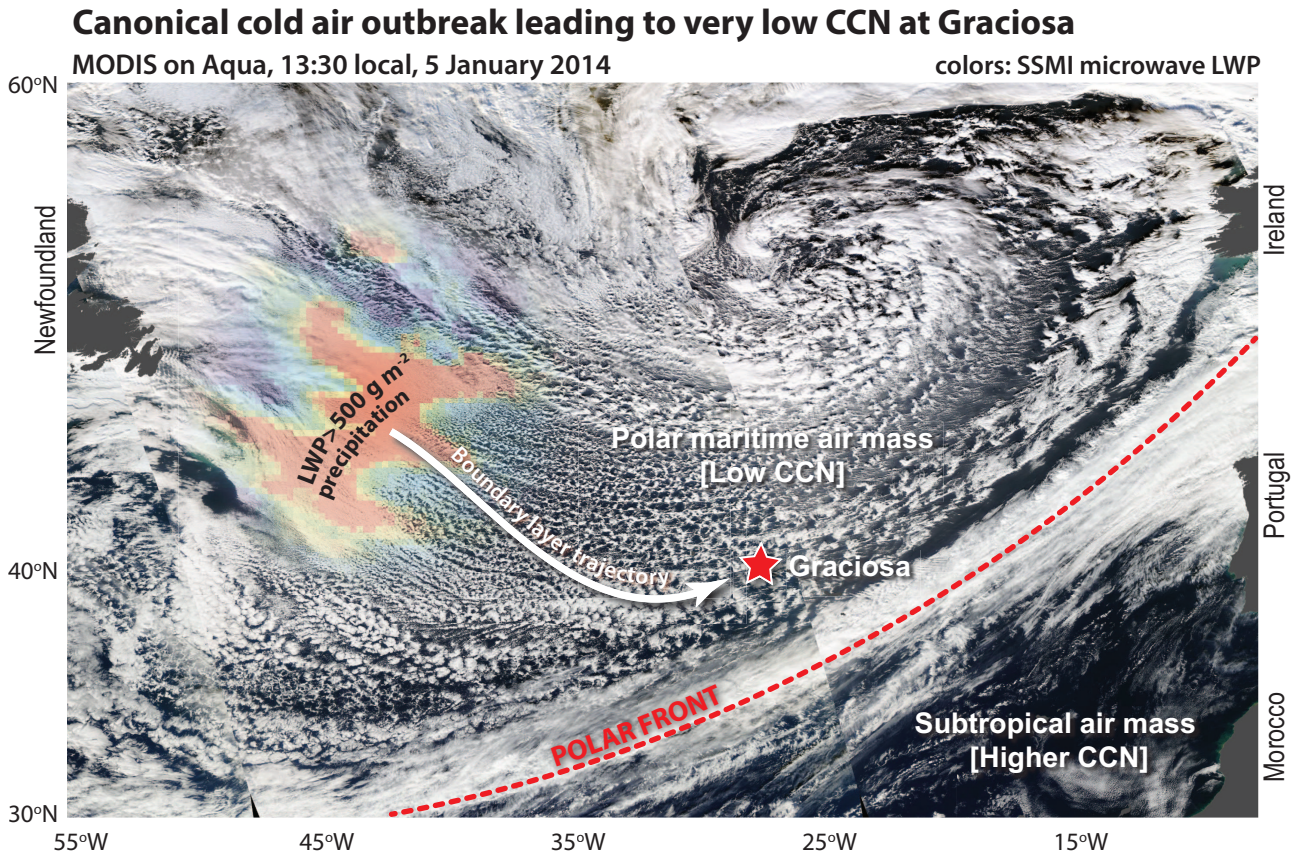


Figure 17. Canonical cold air outbreak case motivating a conceptual model of how precipitating boundary layer clouds can produce very low CCN concentrations at Graciosa. The main image shows a composite of RGB visible imagery from three MODIS swaths from the NASA Aqua satellite ($\sim 13:30$ hr local overpass time) on 5 January 2014 over the North Atlantic. High liquid water path, shown using LWP retrieved earlier that day (06 hr local) from the passive microwave Special Sensor Microwave Imager (SSMI) instrument on the F17 Defense Meteorological Satellite, is found over a broad area (red colors indicate LWP in excess of 500 g m^{-2}) prior to the marine stratocumulus cloud breakup into open cells. In this case, trajectories flowing over Graciosa passed through the region of high LWP 1-2 days prior to arrival. Often, the location of the polar front (red dashed line) delineates the boundary between the very low CCN cold, polar flow from the more CCN-rich subtropical air mass.

Table 1. AMF instruments and data products used in this study

Measurement	Symbol	Instrument/references
Cloud condensation nucleus number concentration at 7 supersaturations S from 0.1-1.2%	N_{CCN}	CCN counter (DMT Model 1) <i>Roberts and Nenes</i> [2005]
CN concentration N_{CN} (all particles larger than 10 nm)	N_{CN}	TSI 3010 counter
Aerosol dry scattering coefficient (450, 550, 700 nm)	σ	TSI 3563 nephelometer
Near-surface wind speed and direction [10 m altitude]	u_{10}	Propeller/vane (RM Young 05103)
Liquid water path	LWP	23.8 and 31.4 GHz microwave radiometers (MWR) <i>Turner et al.</i> [2007]
Cloud droplet concentration	N_d	Narrow field of view radiometer and MWR <i>McComiskey et al.</i> [2009]
Cloud boundaries and types from <i>Rémillard et al.</i> [2012]		Zenith W-band (95 GHz) ARM cloud radar Vaisala ceilometer (CL31)

Table 2. Distinguishing characteristics of low CCN events

Characteristic	low CCN events	non-low CCN conditions
Seasonality	Three-quarters of events during DJF and MAM	Occur all year round
CCN concentrations (0.1%)	median 15 cm^{-3} ; 90% from $5\text{-}25 \text{ cm}^{-3}$	median 80 cm^{-3} ; 90% from $25\text{-}215 \text{ cm}^{-3}$
Aerosol scattering	Low values (both submicron and total) suppressed in approximate proportion to $N_{CCN,0.1\%}$	Larger and more variable scattering
Wind direction (10 m) at Graciosa	Most cases from SW through SE.	Wide range of directions, many from SW clockwise through NW
Wind speed (10 m) at Graciosa	Median wind speed 3 m s^{-1}	Median wind speed 5 m s^{-1}
Back trajectory history	More trajectories experiencing cold air outbreak conditions	Fewer cold air outbreak encounters
Cloud droplet concentration N_d	20-50% lower N_d beginning several days upstream	Higher N_d beginning several days upstream
Liquid water path (LWP)	Little difference at Graciosa, but large values 2-3 days prior to trajectory arrival at Graciosa	Little difference at Graciosa; upstream distributions flat.